# Stimulus Coding and Synchrony in Stochastic Neuron Models

**by**
**Jakub Cieniak**

**Thesis submitted to**
**the Faculty of Graduate and Postdoctoral Studies**
**in partial fulfilment of the requirements for**
**the M.Sc. degree in Physics**

**Department of Physics**
**Faculty of Science**
**University of Ottawa**

*for Kika*

**M***EUS A***M***OR MA***XI***MUS SEMPER TU*

# Contents

# List of Figures

# List of Acronyms

| | |
|---|---|
| AC | adaptation current |
| DT | dynamic threshold |
| EOD | electric organ discharge |
| ER | envelope-response |
| *f-I* | firing rate-intensity (curve) |
| IF | integrate-and-fire (neuron model) |
| ISI | interspike interval |
| ISIH | interspike interval histogram |
| LIF | leaky integrate-and-fire (neuron model) |
| LIFAC | leaky integrate-and-fire (neuron model) with adaptation current |
| LIFDT | leaky integrate-and-fire (neuron model) with dynamic threshold |
| RAM | random amplitude modulation |
| RISE | resonance-induced synchrony enhancement |
| RR | response-response |
| SAM | sinusoidal amplitude modulation |
| SR | stimulus-response |

# Abstract

A stochastic leaky integrate-and-fire neuron model was implemented in this study to simulate the spiking activity of the electrosensory "P-unit" receptor neurons of the weakly electric fish *Apteronotus leptorhynchus*. In the context of sensory coding, these cells have been previously shown to respond in experiment to natural random narrowband signals with either a linear or nonlinear coding scheme, depending on the intrinsic firing rate of the cell in the absence of external stimulation. It was hypothesised in this study that this duality is due to the relation of the stimulus to the neuron's excitation threshold. This hypothesis was validated with the model by lowering the threshold of the neuron or increasing its intrinsic noise, or randomness, either of which made the relation between firing rate and input strength more linear.

Furthermore, synchronous P-unit firing to a common input also plays a role in decoding the stimulus at deeper levels of the neural pathways.

Synchronisation and desynchronisation between multiple model responses for different types of natural communication signals were shown to agree with experimental observations. A novel result of resonance-induced synchrony enhancement of P-units to certain communication frequencies was also found.

# Résumé

Un modèle de neurone stochastique intégre-et-tire à fuite a été utilisé dans cette étude pour simuler l'activité des impulsions de l'unité-P des neurones récepteurs électrosensoriels des poissons faiblement électriques *Apteronotus leptorhynchus*. Dans le codage sensoriel, il a récemment été montré dans des expériences que ces cellules répondent à des signaux à bande étroite aléatoires et naturels avec un programme à codage linéaire ou non-linéaire, dépendamment de la fréquence de décharge de la cellule quand elle n'est pas stimulée par une source externe. L'hypothèse qui a été émise est que cette dualité est causée par la relation du stimulus avec le seuil d'excitation du neurone. Cette hypothèse a été validée avec le modèle en baissant le seuil d'excitation ou en augmentant le bruit intrinsèque, ou le caractère aléatoire, du neurone, l'un et l'autre rendant la relation entre la fréquence de décharge et l'intensité du signal plus linéaire.

De plus, la fréquence de décharge synchrone de l'unité-P en réponse à

un stimulus commun joue aussi un rôle dans le décodage du stimulus à des niveaux plus profonds des voies nerveuses. La synchronisation et la désynchronisation entre les réponses multiples du modèle à différents types de signaux de communication naturels sont en accord avec les observations expérimentales. Un résultat inédit de la synchronie augmentée des unités-P de la résonance à certaines fréquences de communication a aussi été trouvé.

# Acknowledgements

First, I sincerely thank my supervisor Dr. André Longtin and co-supervisor Dr. Leonard Maler for their guidance in this study and their invaluable suggestions for this thesis. I also thank Dr. Jan Benda and Dr. Gary Marsat for providing crucial experimental data, as well as Dr. Jason Middleton and Dr. Maurice Chacron for assistance with the numerical modelling. A special thank-you to Kristin Le Saux-Farmer for translating the abstract into French—*bon job!* Financial support was provided by NSERC and OGS.

Finally, I especially thank my friends and family for their everlasting support and infinite patience, above all my wife, Carolina, to whom this work is dedicated.

# Chapter 1

# Introduction

Neurons are the cellular building blocks of the brain and nervous system that relay information to and from every part of the body via electrical signals. Understanding how they generate these signals and under what conditions is a very important, and relatively recent, area of scientific research [16]. Even more important is determining why the brain sometimes does not function properly, for example due to the deterioration or loss of sensory function such as sight or hearing. Neurophysics is a branch of biological physics that focusses on understanding the dynamics of cellular mechanisms governing the behaviour of neurons and nervous systems.

The physics applied here is the nonlinear dynamics of synchronising excitable systems, that is, systems that are in a state near a transition point, or bifurcation, that can be excited by some external force into a qualitatively

different state. The same amount of force produces the same level of excitation to create synchrony between similar instances of the system receiving the same input. The inputs in this context are sensory stimuli incident on specialised receptor neurons. When the neurons are excited by an appropriate stimulus, they transition from a quiescent state to an active one as they *fire* an electrical impulse, called an *action potential* or *spike*, that propagates to the next cell in the neural pathway. The translation of a stimulus into a sequence of spikes, or *spike train*, is termed *sensory coding*, where the stimulus is encoded into a spike train, which is then decoded by neurons at the next level of neural circuitry and encoded again into their own spike trains. Synchronous firing of multiple neurons also plays a role in decoding the stimulus at deeper levels of the circuitry [22].

This research involves the weakly electric fish *Apteronotus leptorhynchus*, the brown ghost knifefish. These fish inhabit very murky waters and rely almost entirely on their electric sense to navigate, hunt for prey, evade predators, and communicate with other members of their species [1, 28, 23]. Because of this anisotropy in sensory information, these fish have evolved with more isolated neural circuitry than most other animals that process visual, auditory, and olfactory information, which is usually combined to

verify agreement between the different stimuli. The reduced complexity of the electrosensory system in these weakly electric fish and its similarity to the auditory system [6] make this an ideal system for studying general biophysical principles of sensory coding.

The focus of the work presented here is the theoretical modelling and computer simulation of the electroreceptor neurons at the periphery of the electrosensory system, that is, the primary sensors of electric fields at the initial phase of interpreting electric stimuli—the so-called P-units [7]. The goal was to thoroughly investigate the properties of a previously proposed model, and to extend it to reproduce and explain more recent experimental results. Indeed, Benda et al. (2005) showed that short transient communication signals known as small chirps synchronise P-unit responses [3], and again (2006) that longer communication signals, known as large chirps, desynchronise them [4]. The latter effect is shown in Figure 1.1. The synchrony is quantified by the spike correlation, defined in Equation 2.10 (labelled in the figure as 'Single unit correlation') and the chirps occur during a type of stimulus known as a beat signal. The P-units yield significantly lower correlation values at the chirp than for the rest of the beat signal, signifying a loss of synchrony. These results were obtained by recording action potentials from

P-unit afferents *in vivo* with sharp micropipettes inserted into the nerve to measure the potential difference between the micropipette and a reference electrode placed in the fish's neck muscle. It is shown in this study that the model reproduces the results for both types of chirps and the role of an adaptation mechanism is discussed; further, a variant of this model is analysed, in which a different form of adaptation mechanism is invoked to explain experimental results.

Middleton et al. (2006) showed that P-units encode narrowband random amplitude modulated signals with a linear scheme [21], while Savard et al.

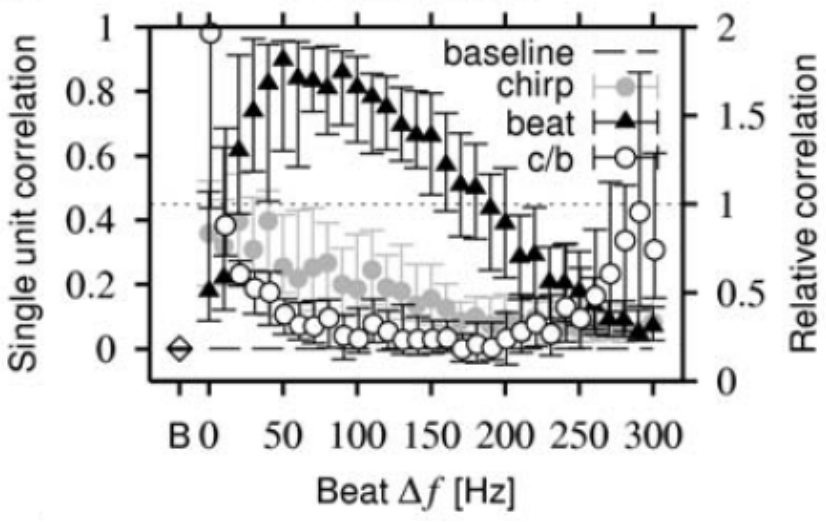


Figure 1.1: Median spike correlation values (labelled 'Single unit correlation') during beats (black triangles) and chirps (grey circles) and their ratio (white circles, right axis) as a function of beat frequency $\Delta f$ for P-units recorded experimentally [4]. The P-units show significant loss of synchrony (lower correlation) during chirps. (Reproduced with permission.)

(2011) showed that P-units with certain properties encode similar signals with a nonlinear scheme [25]; this latter result in fact verifies a prediction made in this thesis and published by Longtin et al. in 2008 [18]. Both of these cases are also reproduced with the model by adjusting appropriate parameters. The choice of parameters is determined by theoretical predictions from analysis of the P-unit's baseline properties, that is, when not receiving any external stimulation.

This work combines a proven computational model for the P-units with a realistic adaptation mechanism and highlights the regions in parameter space where the model responses agree with experimental results, making it a useful tool in predicting neuronal behaviour—and in particular neuronal correlations in firing times—for various types of stimuli.

## Thesis Layout

Chapter 2 provides a more thorough background of the subject matter covered in this work. It describes the properties of neurons and how they are simulated with progressively more advanced models. Two fundamentally different adaptation mechanisms are described and the results they generate are

compared. The various types of input stimuli are described as well as how and when they are encountered by the fish. Finally, the statistics used to measure the output of the P-units are defined.

Chapter 3 details the mathematical model of the cell membrane potential dynamics and outlines its basic functions. The results of an exploration of its parameter space are provided to define the boundaries of appropriate behaviours. Model responses to advanced stimuli are also introduced.

In Chapter 4, the difference between linear and nonlinear coding of input signals is described in detail. Mechanisms for adjusting the level of nonlinearity in the coding properties are suggested.

The synchrony of neuronal responses to communication-type signals is examined in Chapter 5. The effects of varying different parameters on the level of synchrony are explored.

A summary of the results, a discussion of their implications for possible mechanisms responsible for experimental outcomes, as well as ideas for future studies concludes this work in Chapter 6.

# Chapter 2

# Background

## 2.1 Neurons

Neurons are electrically active cells in an animal's body relaying information about the environment coded in electrical signals. These signals are processed and interpreted in ever higher brain centres until a response is determined and relayed in turn to the appropriate cells responsible for the mechanical or chemical function. A typical neuron can be divided into three segments: the dendrites—a tree-like structure of branching tubular filaments at one end of the cell, commonly referred to as the dendritic tree; the soma—the central and largest part of the neuron resembling the cell body of many other types of cells; and the axon—usually another, single filament at the other end of the cell that branches out near target neurons at the next level of information

processing to form multiple *synaptic* connections with their dendrites [13]. An electrical impulse generally propagates through the neuron in that order; that is, a signal is detected by the dendrites, sent to the soma where it is processed, and, if a response is to be elicited, a signal is sent down the axon, which can be entwined by dendrites from many neurons to relay the message. (Sometimes an axon branch will terminate at the soma of another neuron and relay the signal directly to the soma bypassing the dendritic tree altogether.)

The neurons studied here are the *electroreceptor afferents*, also called P-units—a type of sensory neuron—in the weakly electric gymnotiform fish *Apteronotus leptorhynchus*, known as the brown ghost knifefish. The brown ghost is a typically nocturnal fish that lives in murky water and, hence, relies primarily on its electric sense [1, 28, 23]. Because of its limited use of other senses, the electrosensory system of the brown ghost is much less complex than the more "cluttered" compound sensory system of an animal that must decipher a stimulus composed of a combination of visual, auditory and olfactory cues from its surroundings. However, this does not make it a less relevant system to study as it bears many similarities to the auditory system [6] and, since it can be studied virtually entirely independent of other senses, it may be more useful in "eliminating variables" in more complicated

systems, such as, ultimately, that of humans.

## 2.2 Neuron Models

A detailed model of the neuron—such as that defined by Hodgkin and Huxley [16]—could accurately reproduce some of its observed behaviour by describing the intricate, "low-level" dynamics of the ionic channels and transmembrane currents dictating the flow of ions between the inside and outside of the cell producing a potential difference, leading to (under the correct conditions) a sudden discharge of the stored electrical energy known as an *action potential*. However, the dynamics of the build-up and release of electrical potential, or *spiking activity*, can be sufficiently modelled by a simpler non-linear phase oscillator representing the transmembrane voltage difference. Such a model belongs to the class of neuron models referred to as *integrate-and-fire*, where a neuron is said to have *fired* when it undergoes the rapid drop in voltage returning to its initial state after reaching the threshold specific to that neuron (see, for example, [15] and references therein). In fact, properly extended versions of these models better reproduce certain attributes of real neurons, such as memory.

### 2.2.1 Integrate-and-fire

The normalised simple integrate-and-fire (IF) neuron model can be implemented by the following differential equation for the transmembrane potential difference (or voltage) $V$:

$$\tau_V \frac{\mathrm{d}V}{\mathrm{d}t} = I \tag{2.1}$$

$$V(t_{V>V_{\mathrm{th}}}) = 0 \tag{2.2}$$

for an input bias current $I$ (scaled by a standard capacitance value used in neuronal modelling) and membrane potential time constant $\tau_V$ as parameters to the model. (Although $\tau_V$ could be absorbed by $I$ into a single parameter as the ratio between the two is the only degree of freedom, it is useful to introduce the distinction before graduating to more complex models.) As the name implies, in this simple model the neuron accumulates (i.e. *integrates*) electric potential across the cell membrane from the bias current—Equation 2.1—until it surpasses the neuron's intrinsic threshold level $V_{\mathrm{th}}$, at which point the voltage resets to the zero value—Equation 2.2.

The solution to this system of equations is a sawtooth function with slope $I/\tau_V$ and period $\tau_V V_{\mathrm{th}}/I$. This model assumes an infinitely sensitive neuron

that always responds (eventually) to any positive input signal $I$, no matter how small it might be. However, this is not the case in reality as there exists a limiting bias current, known as the *rheobase*, below which no spiking activity is recorded. To account for this finite sensitivity in real cells, a *leak* current proportional to the cell's membrane potential is introduced into the model—the leaky integrate-and-fire (LIF) neuron model is implemented as follows:

$$\tau_V \frac{\mathrm{d}V}{\mathrm{d}t} = -V + I \tag{2.3}$$

with the same threshold condition, Equation 2.2, as in the IF model. Solving gives the inverted exponential decay curve $V(t) = I(1 - e^{-t/\tau_V})$, which increases and approaches the asymptotic value $I$ with decreasing rate governed by the time constant $\tau_V$. Contrary to the IF model, if the bias current is at or below a critical value—in this case the membrane threshold—the LIF model will never fire; however, if the bias is greater than the threshold, the model will produce periodic spiking events with a constant interval of $-\tau_V \ln(1 - V_{\mathrm{th}}/I)$.

To simulate an even more realistic neuron, a stochastic term is included in the differential equation to account for randomness, or noise, in the system

from fluctuations in ionic currents, neurotransmitter levels, etc.:

$$\tau_V \frac{\mathrm{d}V}{\mathrm{d}t} = -V + I + \sigma\xi(t). \tag{2.4}$$

Here, $\xi(t)$ is zero-mean, unit-variance Gaussian white noise (that is, random samples from a normal distribution with mean zero and variance one); the parameter $\sigma$ scales the noise intensity to provide an adjustable distribution with an effective variance of $\sigma^2$.

To implement a real environment with natural signals normally encountered by the receptors, the input current $I$ need not be constant: its variation over time can be described for various types of stimuli, as discussed at the end of this section, with explicit formulas for modelling given in the following chapter.

### 2.2.2 Adaptation

An important characteristic of certain neurons such as the P-units is the ability to adapt to an unchanging level of stimulation (see, for example, [12, 9, 2] and references therein). This *adaptation* to a constant input is characterised in the neuron by a gradual decrease in spiking activity, whereby

the neuron tends to produce action potentials less frequently than at the onset of the novel stimulus eventually reaching some equilibrium or steady state. This effect can be described quantitatively by measuring the time interval between successive action potentials, or *interspike interval* (ISI), and observing a steady increase towards an asymptotic value. Alternatively, this can be equally demonstrated using the inverse relation by computing the instantaneous firing rate of the neuron as the reciprocal of the ISI to show a steady decline. Figure 2.1 shows an example where this criterion is met.

This is not to say that these neurons are simply novelty detectors and convey no information about the detailed structure of the input signal. In fact, the relative strength or intensity of the signal is transmitted by the initial firing rate of the neuron at the onset of the novel stimulation based on the previous, or *pre-adaptation*, input to which the neuron had adapted. Figure 2.2 illustrates this firing rate-intensity ($f$-$I$) relation by way of the so-called *f-I curves* for a deterministic (i.e. non-stochastic) model of the P-unit neuron using two different implementations of the adaptation mechanism: a dynamic threshold and an adaptation current (explained in detail in the following chapter). It is known ([2, 5] and references therein) that the linear part of the curves (towards higher input strengths) are parallel as in the

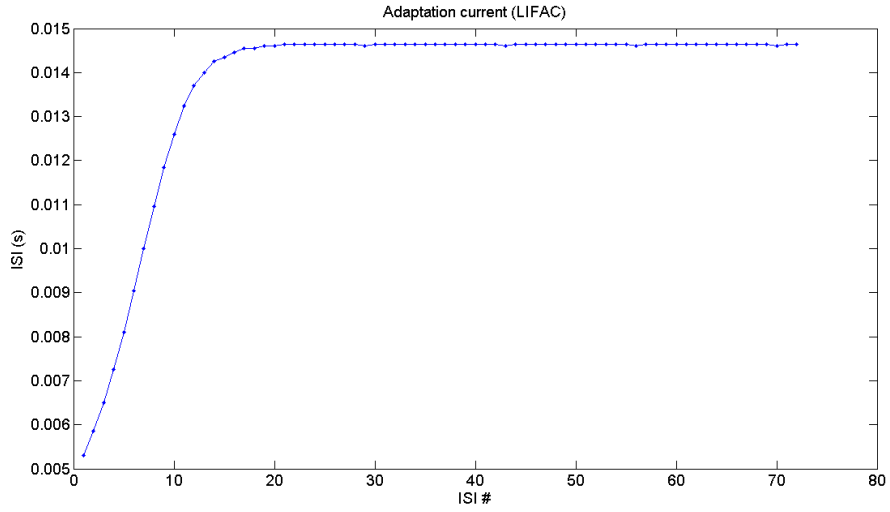


A

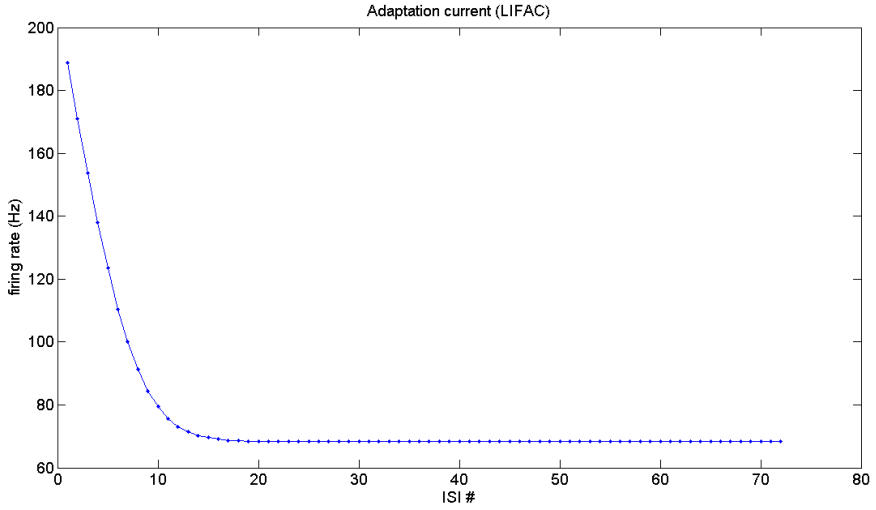


B

Figure 2.1: P-unit model adaptation to a constant stimulus is shown by (A) increasing interspike intervals or, equivalently, (B) decreasing firing rate after stimulus onset. (Data generated by LIF model with adaptation current, Eqs. 3.7, 3.8.)

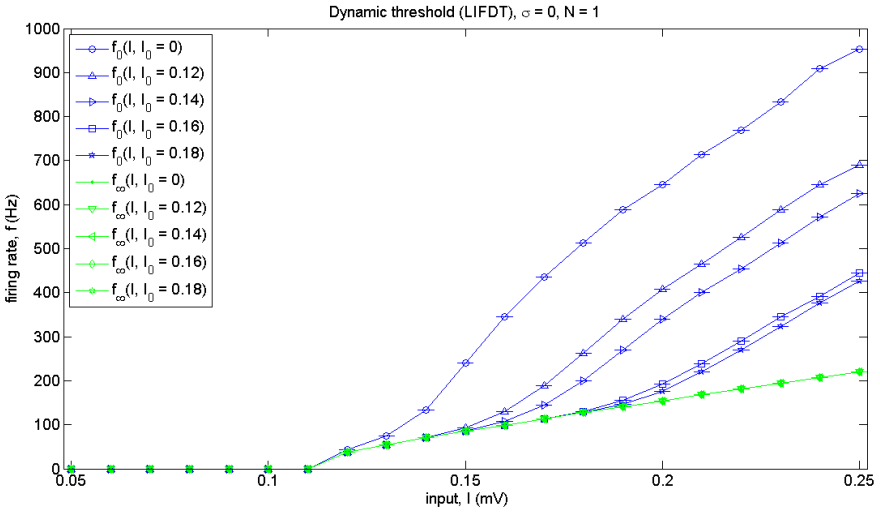


A

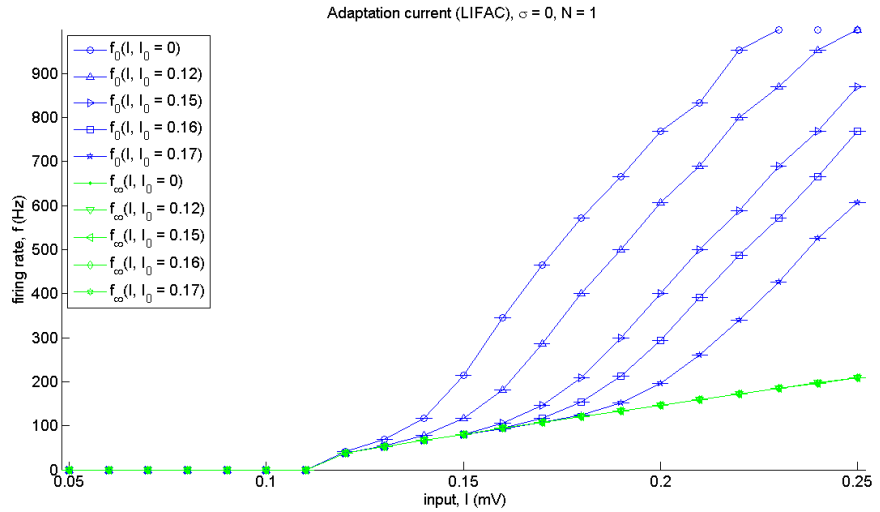


B

Figure 2.2: $f$-$I$ curves of deterministic P-unit model (no internal noise: $\sigma = 0$) with (A) dynamic threshold (Eqs. 3.1, 3.6) and (B) adaptation current (Eqs. 3.7, 3.8), showing onset ($f_0$) and steady-state ($f_\infty$) firing rates for various pre-adaptation states (defined by initial input $I_0$).

model with adaptation current (Figure 2.2B), and not of varying slopes as with the dynamic threshold (Figure 2.2A).

### 2.2.3 Types of Input

The natural underlying input signal incident on the electroreceptors is, for the most part, the electric field generated by the fish's own electric organ discharge (EOD) rhythm or, as is more relevant to the purpose of the electric *sense*, the distortions of this field by electrical entities in the fish's environment such as obstacles, prey and predators as well as conspecifics (other fish of its kind), with which a more complex combination of signals is encountered, as described below. This perturbation of the electric field alters the signalling behaviour of the receptors and is the source of the fish's *active* electrolocation (as opposed to the *passive* form, which requires only detection of electric fields and not their production—such as in the case of sharks or catfish) [1, 19]. Two classes of weakly electric fish exist with respect to their EOD signal: *wave-type* fish emit a periodic, quasi-sinusoidal EOD signal—at a particular frequency for each fish—that remains constant a vast majority of the time for most of the fish's life; the EOD of a *pulse-type* fish, on the other hand, varies continually from short pulses separated by long intervals

of silence to fast bursts of activity. *A. leptorhynchus* belongs to the former class.

When two wave-type electric fish are near each other so that their electric fields overlap, a linear combination of their EOD signals results at the receptors based on the relative strengths of their respective signals and their separation distance. In an effect identical to that when audio signals coincide, a *beat* signal is produced with a frequency equal to the difference in frequencies of the EOD signals. This signal can be seen as a sinusoidal amplitude modulation (SAM) of the EOD of the fish being tested with a modulation rate equal to this *beat frequency*. The P-units synchronise strongly at certain values of the beat frequency showing peaks in spike correlation values (defined below) when graphed against frequency, each one with a slightly different shape of the graph depending on its baseline characteristics.

Although the sensory neurons can generate elaborate response patterns to the various beat signals the electric fish encounter, the *behavioural* response of the fish themselves is generally to destroy the beat signal by producing a "brief frequency excursion" in their normally constant-frequency EOD signal, also known as a *chirp*, believed to be a form of active communication between some species of weakly electric fish [3, 4]. This phenomenon will be further

analysed in a later chapter.

When many fish are together, as they prefer to do naturally—usually about 6–8 in a group—a spectrogram of a signal reading in the area reveals a narrowband signal composed of frequency differences between the EODs of all fish. In an attempt to define in which situations the P-unit model behaves *linearly* or not when coding the information in a setting such as this (explained in detail in a later chapter), a narrowband stimulus is generated from filtered Gaussian white noise and presented to the neurons as a random amplitude modulation (RAM) of the basic EOD signal. It was believed that these cells are linear [27, 26] and cannot encode the signal's underlying *envelope* (a nonlinear attribute [21, 11]). However, very recently it was shown that some of the cells are *nonlinear* and can, in fact, encode the nonlinear envelope [25]. The envelope $E(t)$ of a signal $S(t)$ is computed as the magnitude

$$E(t) = \left|S_{\mathrm{a}}(t)\right| = \sqrt{S^2(t) + \widehat{S}^2(t)} \tag{2.5}$$

of the analytic representation $S_{\mathrm{a}}(t) = S(t) + i\widehat{S}(t)$ of the signal $S(t)$, where the imaginary part $\widehat{S}(t) = \mathcal{H}[S](t)$ is the 90° phase shift of the real frequency

components of $S(t)$ known as the Hilbert transform [21]:

$$\mathcal{H}[S](t) = \frac{1}{\pi}\mathcal{P}\int_{-\infty}^{\infty} \frac{S(\tau)\,\mathrm{d}\tau}{t-\tau}. \tag{2.6}$$

Here, $\mathcal{P}$ indicates taking the Cauchy principle value of the improper integral that follows it.

Of course, what is of real interest in these studies is the *output* from the neurons. Even though the model implements the cell's responses to stimuli through its membrane potential dynamics, the main focus of the analyses presented here will be on the neuron's spiking activity and patterns therein. The set of action potentials from a given neuron over a specified period of time is known as a *spike train*. This response, $R(t)$, can be described analytically as a series of Dirac delta functions shifted to the spike times $t_i$ in the response:

$$R(t) = \sum_{i=1}^{N} \delta(t - t_i), \tag{2.7}$$

where $N$ is the number of spikes over the entire time period considered. For discretised numerical computations that only need to consider whether an action potential took place or not, this can be implemented simply as an array of single binary digits (or *boolean* values) representing each integration

timestep taking on the value 1 (or *TRUE*) if a spike occurred during that time and 0 (or *FALSE*) otherwise.

## 2.3 Statistical Measures

To describe and compare the spiking activity of the electroreceptor neurons, order-dependent statistics such as coherence and correlation as well as order-independent statistics such as histograms are calculated from the spiking data acquired from the experimental or simulated runs.

### 2.3.1 Firing Rate

The firing rate of the neuron is one of the most important pieces of data calculated as it quantifies the activity of the cell describing how it responds to different levels of stimulation. Two flavours of the firing rate are considered when analysing the response of the neuron to a particular stimulus: the instantaneous firing rate and the mean firing rate. The instantaneous firing rate is computed for the time interval between any two successive spiking events by calculating the reciprocal of the difference in spike times of the two events, or simply the reciprocal of the interval duration (just as the

reciprocal of the period of a cyclic event yields its frequency). Successive values of the instantaneous firing rate describe how the spiking activity of a neuron changes over time, due to a change in the stimulus, for example.

A mean firing rate describes the general behaviour of a neuron to some constant stimulus (or a periodic stimulus with a constant frequency) and is found by computing the average value of the instantaneous firing rate over the entire time period of interest or, equivalently, by summing the number of spikes during that time period and dividing by its duration.

The natural range of observed firing rates in P-units follows a lognormal distribution [14]. The reasons for this are not yet understood.

### 2.3.2 P-value

The defining characteristic of each P-unit is the probability that it will fire during a given cycle of the fish's EOD signal while receiving no external stimulation; the measure of this *baseline* activity is called the p-value. (In fact, the P-unit's name is derived from its probabilistic nature.) The p-value defines a neuron because it does not change for the life of the cell so long as it remains healthy and because neurons of the same type that have similar p-values will exhibit similar behaviour when encountering the same stimulus.

Because of its linear relation to the firing rate, this measure is also log-normally distributed in real cells [14].

### 2.3.3 Interspike Interval Histogram

An ISI histogram (ISIH) of the time intervals between successive spiking events is used very frequently to make qualitative comparisons of the distribution of the ISIs from one neuron to the next or for varying stimuli or from simulated to experimental responses; a quantitative comparison of the means and modes of the distributions is also a very useful tool.

### 2.3.4 Interspike Interval Serial Correlation

A serial correlation of a signal, or *autocorrelation*, reveals any dependency of the values on other values in the series due to some underlying pattern in the signal. In particular, it is useful for measuring how strongly the values depend on previous values and can indicate how well following values can be predicted, if at all. The ISI correlation coefficients for intervals $\tau$ at lag (or separation) $n$ are defined by

$$c_{\mathrm{ISI}}(n) = \frac{\left\langle \tau_m \tau_{m+n} - \left\langle \tau_m \right\rangle^2 \right\rangle}{\left\langle \tau_m^2 - \left\langle \tau_m \right\rangle^2 \right\rangle}, \tag{2.8}$$

where values inside angle brackets, $\langle\rangle$, are averaged over index $m$ [10]. At lag 0, $c_{\mathrm{ISI}}(0) = 1$ by definition. For an infinite sequence of independent and identically distributed ISIs, it is referred to as a *renewal process*, that is the values have no memory of previous values, and $c_{\mathrm{ISI}}(n) = 0$ for $n > 0$. If $c_{\mathrm{ISI}}(n)$ is nonzero for any $n > 0$, it is no longer a renewal process as there is memory in the sequence from dependence on previous values.

### 2.3.5 Phase-locking

The ability of a forced oscillator, such as a stimulated neuron, to cycle in unison, or *synchronously*, with its driving force to within a constant phase difference is known as *phase-locking*. A histogram of the phase of the stimulus when the neuron completes a cycle, say at an action potential, shows the distribution of the relative phase difference between the two signals. The mode measures the most likely time (or times if there are multiple modes) that the neuron will fire during a cycle of the stimulus and can indicate the delay until the neuron responds to the signal, or *encodes* the information from it. The spread of the data about the mode indicates how faithfully the neuron encodes the stimulus and how useful it is at obtaining relevant information from the given type of signal.

### 2.3.6 Coherence

Coherence is another measure of the fidelity with which the electroreceptors transmit information about the presented stimulation to higher brain centres and the degree of *linearity* with which they encode it. This function of frequency is used in this study to analyse the response of the P-units to RAM signals. It is given by

$$C_{\mathrm{SR}}(f) = \frac{\left|P_{\mathrm{SR}}(f)\right|^2}{P_{\mathrm{SS}}(f)P_{\mathrm{RR}}(f)} \tag{2.9}$$

for the power spectral densities $P_{\mathrm{SS}}(f)$ of the stimulus and $P_{\mathrm{RR}}(f)$ of the response (i.e. spike train) and their cross-spectral density $P_{\mathrm{SR}}(f)$ and ranges from 0 (no linear encoding) to 1 (perfect linear encoding) [20, 18].

### 2.3.7 Spike Correlation

One way to measure the extent of synchronisation between neurons (or between repeated readings—called *realisations*—of the same neuron) subjected to the same stimulus is to compute the correlation coefficient $r$ between two

spike trains $s_1(t)$ and $s_2(t)$ as follows [4]:

$$r = \frac{\langle (s_1 - \langle s_1 \rangle_t)(s_2 - \langle s_2 \rangle_t) \rangle_t}{\sqrt{\langle (s_1 - \langle s_1 \rangle_t)^2 \rangle_t \langle (s_2 - \langle s_2 \rangle_t)^2 \rangle_t}}, \tag{2.10}$$

where values inside angle brackets subscripted with $t$, $\langle \rangle_t$, are averaged over time and these spike trains are $R(t)$ (Equation 2.7) convolved with Gaussian kernels of 1 ms standard deviation. If several neurons (or realisations) are recorded, the average correlation coefficient over all distinct pairs of spike trains is computed and is referred to as the *spike correlation* for the particular stimulus and neuron characteristics.

# Chapter 3

# Neuron Model

## 3.1 Theory

The theoretical model examined here is an extension of the stochastic LIF model presented earlier. The membrane potential dynamics are [7]

$$\tau_V \frac{\mathrm{d}V}{\mathrm{d}t} = -V + I\big[1 + \sigma\xi(t)\big] \tag{3.1}$$

with the generalised input signal $I$ given by

$$I = \beta(t)\big[S(t) + A_0\big]\,\max\big[0, \sin(2\pi f_{\mathrm{EOD}} t)\big] + B \tag{3.2}$$

where

$$\beta(t) = 1 - c\sin(2\pi\Delta f t) \tag{3.3}$$

is a beat signal with frequency $\Delta f$ and contrast (or relative strength) $c$. $S(t)$ is filtered Gaussian white noise (a type of input described later) with a narrow passband typically in the 40–60-Hz range, which is offset by the baseline amplitude $A_0$. Note that the beat signal $\beta(t)$ and the narrowband signal $S(t)$ are never used simultaneously: either the beat contrast $c$ or the standard deviation of $S(t)$ is set to zero. The next term is the sinusoidal approximation of the fish's EOD signal with frequency $f_{\mathrm{EOD}}$; the *max* function rectifies this signal since the first term, 0, is greater than the negative portions of the sine wave. Only positive voltage deflections are thought to increase the rate of release of excitatory neurotransmitter across the P-unit to afferent axon synapses in the skin [9]. The final term is the signal bias $B$, which represents an internal bias in the cell altering its sensitivity and hence its mean firing rate.

The noise term in Equation 3.1 is slightly different from the one seen earlier: $\xi(t)$ is still Gaussian white noise and $\sigma$ its standard deviation, however if the bracketed term were expanded, it would show an additional term $I$, the input signal, multiplying it as well. This is an example of *noise-coded input*, where the noise magnitude is proportional to the signal magnitude [17]. This small change makes the model more realistic and does not seem to change

its firing behaviour to input significantly.

### 3.1.1 Numerical Integration

To simulate the neuron dynamics, the Euler–Maruyama method was implemented with time step $\Delta t = 0.05$ ms to integrate the stochastic differential equation 3.1 and obtain an approximate numerical solution [26]. Because Gaussian white noise is involved, special care must be taken to obtain accurate numerical results, especially when seeking correspondence with theory. However, this comes at a price: the Euler–Maruyama method is of order $\frac{1}{2}$, so it takes a longer time to integrate (shortening the time step by a factor of 4 leads to an increase in accuracy by only a factor of 2). The discretisation must be implemented by representing the Gaussian white noise in terms of the "derivative" of the Wiener process, $W$ (although this is not a true derivative since $W$ as an analytic function is not differentiable):

$$\tau_V \frac{\Delta V_i}{\Delta t} = -V_{t_i} + I_{t_i} \left( 1 + \sigma \frac{\Delta W_i}{\Delta t} \right). \tag{3.4}$$

The subscript $i$ indicates the index of the discretised time variable and the differences $\Delta V_i$, $\Delta t$, and $\Delta W_i$ are forward differences, so, for example, $\Delta W_i =$

$W_{t_{i+1}} - W_{t_i}$. The Wiener process is defined to have independent increments $\Delta W_i$ identically distributed like the Gaussian distribution with mean zero and variance equal to the corresponding increment in time. To represent this, a random variate $z_{t_i}$, which is typically generated in simulation from a standard normal distribution, must be scaled by the square root of the integration time step. For a constant time step $\Delta t = t_{i+1} - t_i$ and some initial value $V_{t_0} = V_0$ the iterated solution becomes

$$V_{t_{i+1}} = V_{t_i} + (-V_{t_i} + I_{t_i})\frac{\Delta t}{\tau_V} + \sigma I_{t_i}\frac{z_{t_i}\sqrt{\Delta t}}{\tau_V}. \tag{3.5}$$

The simulated "experiments" of this study often involve averaging across multiple simulation executions, or *runs*, that use their own unique sequences of random variates; each such simulation is called a *realisation*.

### 3.1.2 Implementing Adaptation

The implementation of the adaptation mechanism in the P-unit model was briefly discussed in the background to this field of study and, as mentioned earlier, two distinct forms were examined in this particular study: the dynamic threshold (DT) and the adaptation current (AC). However, this mech-

anism was initially modelled in the electroreceptor via the dynamic threshold and was only later replaced by the adaptation current towards the end of the study; therefore, most of the results presented here describe the model incorporating the former implementation, whereas the latter would be used in future studies as it improves upon one aspect of the spiking behaviour of the neuron while the rest remain consistent. Because of this consistency, the analysis of this model remains valid and valuable even without the enhancement to the adaptation mechanism.

Looking back at Figure 2.2, the $f$-$I$ curves depicting the two forms of adaptation may appear to be similar at first glance differing only quantitatively in their firing rates for corresponding input stimulus intensities, however, there is a significant qualitative difference between the two sets of curves expressed in the relative slopes of the curves in each set. With the DT method the slopes of the onset $f$-$I$ curves tend to decrease as the pre-adaptation input $I_0$ increases—this is called a *divisive* effect since the increasing input essentially divides the values of each successive curve. Conversely, for the AC method the slopes of the onset curves tend to stay constant for varying input, however the values themselves decrease for increasing pre-adaptation input—what is termed a *subtractive* effect. In nature, it is this latter effect

that appears predominantly in these types of experiments [5].

The mathematical model for the P-unit's adaptation implemented with a dynamic threshold $\theta$ is

$$\tau_\theta \frac{\mathrm{d}\theta}{\mathrm{d}t} = \theta_0 - \theta + \Delta\theta\delta(t - t_{V>\theta}) \tag{3.6}$$

where a threshold increment $\Delta\theta$ creates a step in the threshold integration at the time $t_{V>\theta}$ of a positive-going threshold-crossing by the membrane potential $V$. Optionally, as explored later, a "jitter" can be incorporated into this step value as a random Gaussian variate with a standard deviation $\sigma_{\Delta\theta}$ relative to the step, replacing $\Delta\theta$ with $\Delta\theta\big[1 + \sigma_{\Delta\theta}\xi_{\Delta\theta}(t)\big]$ in Equation 3.6.

The implementation of an adaptation current $a$ is given by

$$\tau_a \frac{\mathrm{d}a}{\mathrm{d}t} = -a + \Delta a\delta(t - t_{V>\theta_0}) \tag{3.7}$$

which increments the current by an amount $\Delta a$ when the potential crosses the static threshold $\theta_0$. For this model, the adaptation current is fed into the membrane potential dynamics as a type of input signal, though this signal can be thought of as inhibitory rather than excitatory since it tends

to suppress spiking activity—the potential dynamics now read

$$\tau_V \frac{\mathrm{d}V}{\mathrm{d}t} = -V - a + I\big[1 + \sigma\xi(t)\big]. \tag{3.8}$$

## 3.2 Standard Baseline Activity

The output, or *behaviour*, of the neuron model without any external input signals is termed the *baseline activity*. Figure 3.1 demonstrates this behaviour and some statistics that define the P-units for model parameters that simulate a "standard" or typical neuron. The standard parameter values are chosen from suggested values in previous studies to produce typical baseline behaviour. The top half of the set of sub-figures (3.1A–C) shows a realisation of the deterministic P-unit model, that is, without noise, compared with the stochastic model in the bottom half (3.1D–F).

The first figure in each set (3.1A and D) shows traces of the membrane potential and the dynamic threshold for a portion of a 100-second simulation—the reset of the potential and the step increase of the threshold are clearly visible when the two traces meet. At a quick glance, the two plots may not look too dissimilar especially since the average firing rates are very close for

the two cases. However, with closer inspection the timing of the action potentials might appear less constrained in the stochastic model, as could be expected.

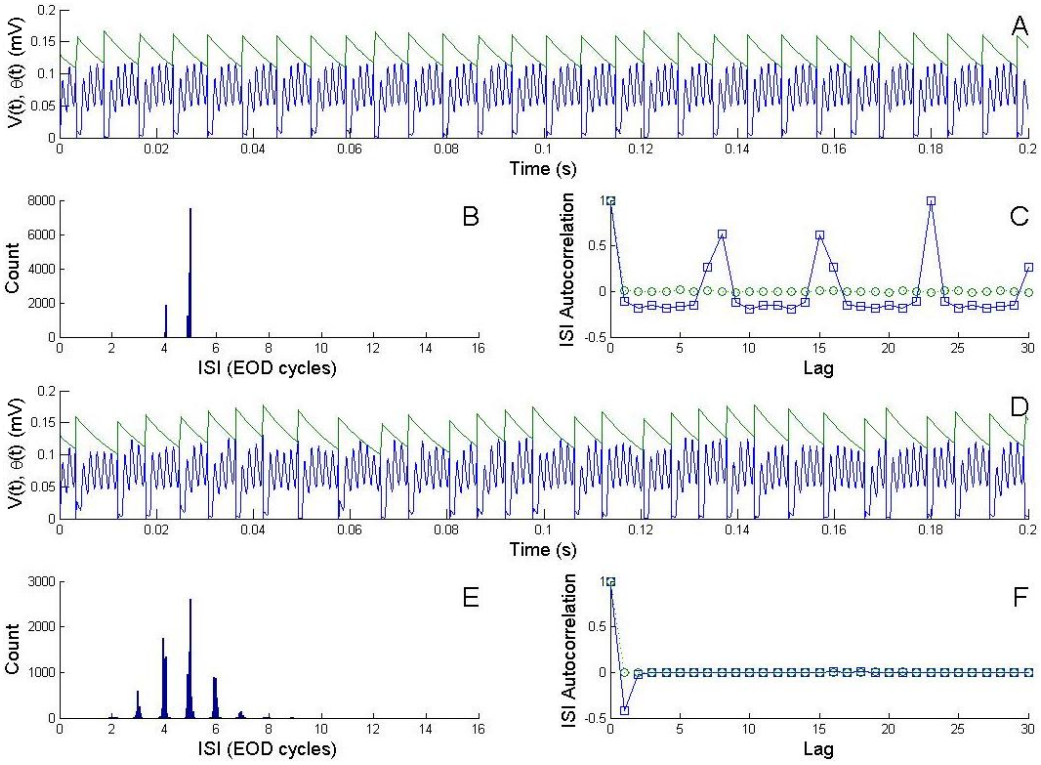


Figure 3.1: Baseline activity and statistics of the leaky integrate-and-fire with dynamic threshold model of a P-unit of a weakly electric fish (Eqs. 3.1, 3.6). (A–C) No internal noise ($\sigma = 0$). (D–F) Internal noise intensity $\sigma = 0.002$. (A,D) Sample of a 100-s simulation of the membrane potential $V(t)$ (bottom curve) and the threshold $\theta(t)$ (top curve). (B,E) Histogram of interspike interval (ISI) measured in EOD cycle duration. (C,F) Serial correlation of ISIs (squares) and shuffled ISIs (circles). Parameters used: $\tau_V = 1$ ms; $\tau_\theta = 14.5$ ms; $f_{\mathrm{EOD}} = 700$ Hz; $A_0 = 0.2613$ mV; $B = 0$ mV; $\theta_0 = 0.03$ mV; $\Delta\theta = 0.05$ mV; $\sigma_{\Delta\theta} = 0$. Contrast of beat signal and standard deviation of narrowband signal are zero.

This observation is verified by the next plot in the set (3.1B and E), showing a histogram of the interspike intervals, with the much smaller spread of ISI values compared with that of the noisy model (albeit with a similar average).

A comparison of the final plots (3.1C and F) demonstrates one of the more characteristic properties that define the behaviour of the P-units. A plot of the ISI serial correlation for the deterministic model shows a lot of structure implying periodicity and long-range predictability (in fact, the model repeats every 23 spikes, which is confirmed by the perfect autocorrelation score at lag 23). In actuality, real P-units are far less predictable and analysis of their ISIs will produce a plot very similar to the one generated by the model incorporating noise: no significant correlation at any lag greater than one and *negative correlation at lag one* [9, 8]. This implies a very short-range, moderate predictability that shorter-than-average ISIs will tend to be followed by longer ones and vice versa. A truly random sequence of ISIs would have no predictability at any lag, which is demonstrated by the circle data points in both plots computed from randomly shuffling their respective ISI sequences.

## 3.3 Exploring Parameter Space

The next step in the analysis of the stochastic LIF neuron model is to explore its behaviour for specific ranges and at specific values of its various parameters. A "standardised" set of measurements are plotted for Figures 3.2 through 3.9 in this section. In the left column of plots: the top pane displays the spike correlation (Equation 2.10) between multiple realisations of the model with identical parameters; the middle pane shows the mean firing rate averaged over the entire realisation; and the bottom pane plots the ISI correlation (Equation 2.8) at the critical lag-1 position. The preceding are all plotted against the parameter being varied. In the second column is a series of full ISI correlation plots for each parameter value to verify the lack of memory in the sequence of ISIs after the first lag. In the third column is a series of ISI histograms for each parameter value. Finally, the right column shows the series for the EOD phase-lock, which are histogram plots displaying the distribution of the phase within the EOD cycle at which a spike is generated.

### 3.3.1 Varying EOD Frequency

In Figure 3.2, the first parameter space to be explored is that of the EOD

frequency, which identifies a particular electric fish; the range chosen has the same limits observed in real brown ghosts, 700–1000 Hz. As would be expected with no external input signal, there is no significant spike correlation between independent runs of the simulation (note the $10^{-3}$ multiplicative factor just above the y-axis and the apparently random positioning of data points that simply fluctuate about zero). This makes sense as the different

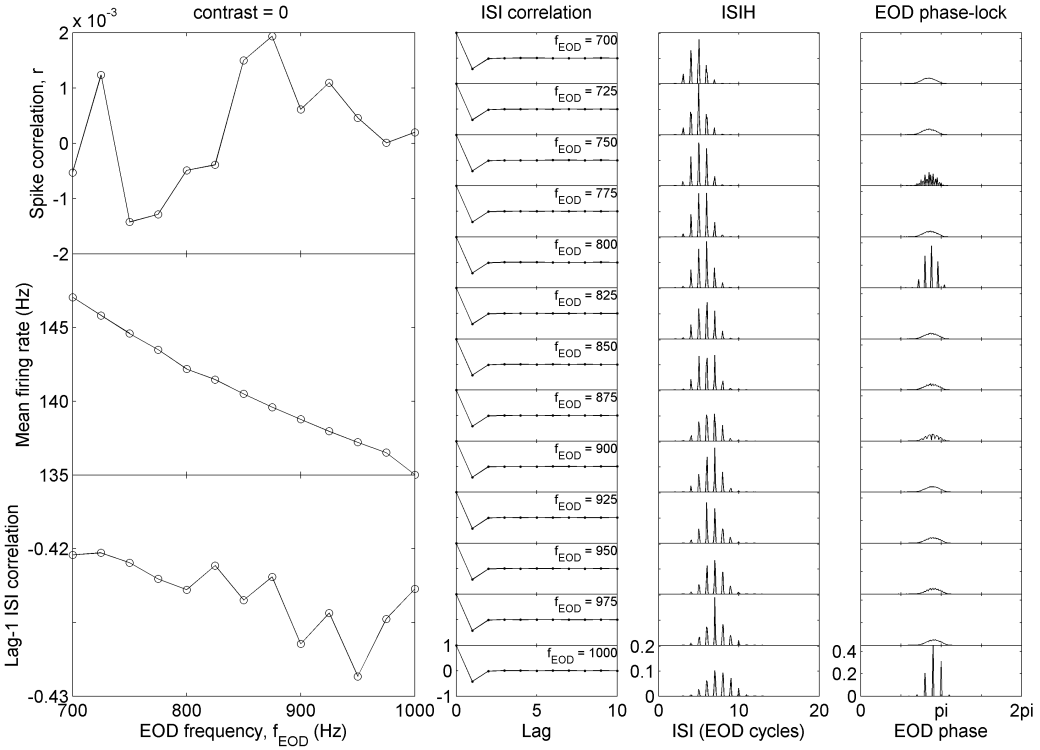


Figure 3.2: Baseline statistics of the stochastic ($\sigma = 0.002$) leaky integrate-and-fire with dynamic threshold model (Eqs. 3.1, 3.6) as a function of EOD frequency $f_{\mathrm{EOD}}$ (Hz; other figures in this section at 900 Hz). All other parameters as in Fig. 3.1. All histograms normalised to 1 and plotted on the scales shown in bottom subfigures.

runs use independent sequences of random numbers, so the firings occur on different EOD cycles in general for each run. The firing rates remain in a fairly limited range, though there is a slight decline of about 12 Hz from 147 to 135 Hz over the entire range of EOD frequencies (which amounts to less than 10% variation). The lag-1 ISI correlations do not vary much over the frequency domain, with all values falling within the experimentally plausible range of $-0.43$ to $-0.42$. Furthermore, the expected lack of memory after the first lag is verified for each value of the frequency in the adjacent ISI correlation plots. In the ISIH series that follows, the distributions of ISIs shift slowly towards larger values. Although this would correspond appropriately to the slight decrease in mean firing rate as EOD frequency increases, this trend is exaggerated in the plots as the shift in the means is mostly a result of the changing unit size in which the ISIs are plotted: the EOD cycles, or periods, are reduced nearly in half over the frequency range explaining the rise in mean ISI from just under 5 EODs to just over 7. As for the EOD phase-locking, the majority of frequency values produce smooth distributions similar to those found in experiment, whereas at a couple of them, such as 750 and 875 Hz, some values of the phase are less favourable than others. At a couple others still, namely 800 and 1000 Hz, a kind of resonance is

present indicating ranges of phase values that are strictly forbidden with only a select few discrete values permitted. This is likely a consequence of phase locking—itself a manifestation of nonlinearity—that occurs on a fine time scale for certain values of the forcing EOD frequency. Worthy of note, too, is that the mean phase as well as its spread remain constant over the range.

### 3.3.2 Varying Bias

Figure 3.3 shows the baseline statistics of the model exploring the bias parameter subspace as it is varied from $-0.10$ to 0.26 mV to generate a realistic range of firing rates. Again, the spike correlation is merely an insignificant, random fluctuation about zero, as expected. The mean firing rate, on the other hand, is quite the opposite: a wide range from almost no firing to a rate of over 400 Hz and a very consistent, nearly linear relation to the bias. This strong dependence on the bias is due to its comparable values to the EOD amplitude, which is the main, in fact the only, stimulus received by the neurons—the bias is essentially a second input into the model, albeit a constant one. The distributions of ISI lengths decrease in their means accordingly, as do their variances as the number of probable values quickly

diminishes. The ISI correlation at lag-1 remains negative for the range of bias values, although it fluctuates significantly and with some underlying pattern: it has a global minimum of $-0.42$ around 0 mV and another local minimum near 0.18 mV and a maximum value of about $-0.1$ at both ends of the range. The extended ISI correlation plots also show a slight trend towards negative values at lags larger than one for positive values of the bias. The EOD phase-lock progressively shifts towards smaller values of the phase

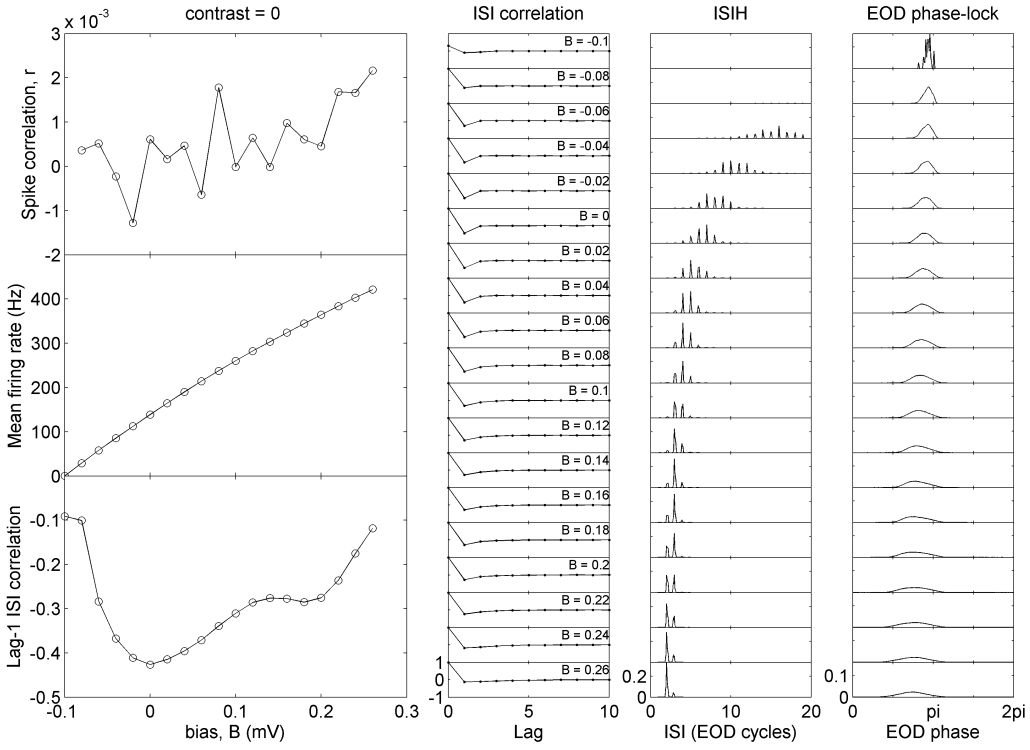


Figure 3.3: Baseline model statistics varying input bias $B$ (mV; standard value is 0 mV) at EOD frequency $f_{\mathrm{EOD}} = 900$ Hz. All other parameters as in Fig. 3.2.

and spreads out to about double its initial range; that is, the neuron tends to fire earlier in the EOD cycle but with greater variability. The discrete look of the EOD phase-lock at a bias of $-0.1$ mV is due to the very small number of events populating the histogram.

### 3.3.3 Varying Bias at 15% Threshold Increment Jitter

In Figure 3.4, the same parameter space is explored again, however this time an alternate value for another parameter is chosen: threshold increment jitter $\sigma_{\Delta\theta}$ is set to 15% as the bias is varied from $-0.1$ to 0.3 mV. Note that in previous plots this parameter was set to zero; the reason for introducing it is based on the synchrony of the P-unit model responses, discussed in a later chapter. The main effect of this added source of noise is to reduce the ISI correlation in magnitude; everything else stays as it was with the previous exploration of the bias subspace.

### 3.3.4 Varying Bias at 30% Threshold Increment Jitter

Threshold increment jitter was raised further to 30% for the same range of bias values again; the results are shown in Figure 3.5. Again the ISI correlations shift upwards, however now their signs switch at 0.16 mV as

consecutive intervals become *positively* correlated, meaning that larger-than-average ISIs tend to be followed by large ones and smaller ones tend to be followed by small ones. The rest of the statistics remain unchanged.

### 3.3.5 Varying EOD Frequency at High Bias

The EOD frequency space is revisited in Figure 3.6, now for a high level of

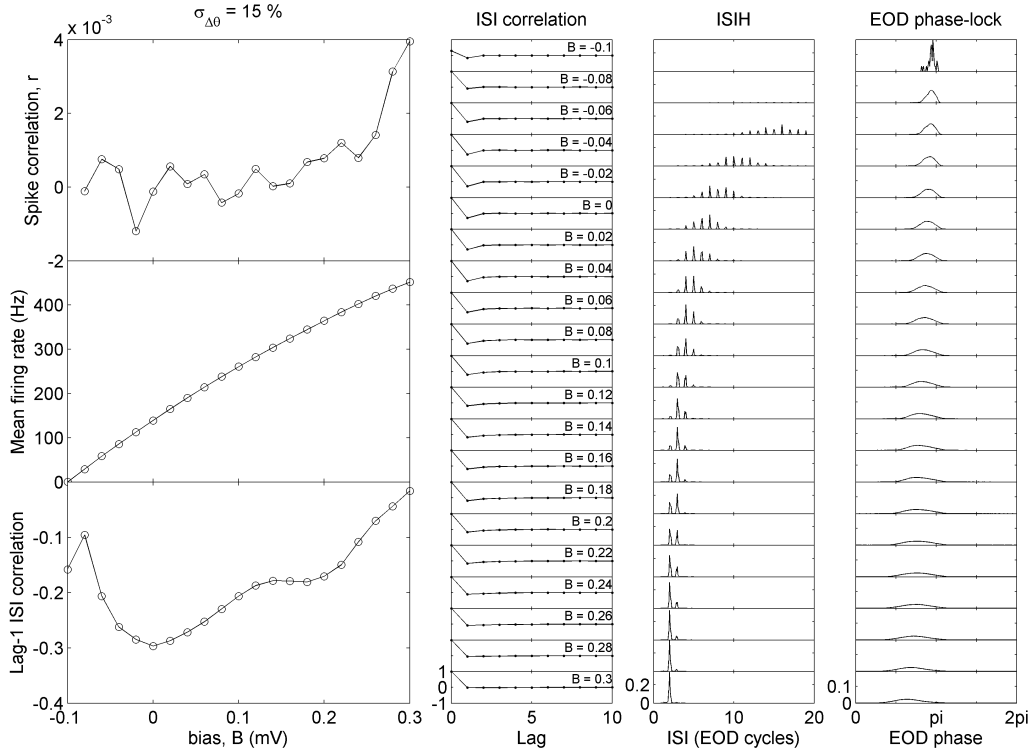


Figure 3.4: Baseline model statistics varying input bias $B$ (mV; standard value is 0 mV) at 15% threshold increment jitter ($\sigma_{\Delta\theta} = 0.15$). All other parameters as in Fig. 3.3.

input bias (0.3 mV instead of 0 as in Figure 3.2). Here the behaviour at a frequency of 900 Hz stands out in several places. It shows up at the top of a peak among very weakly positive spike correlations (all less than 0.01). The range of the mean firing rates is relatively very small (449–456 Hz), though there is a discernible shape to the curve with an inflection point near 900 Hz preceded by a minimum at 850 Hz and followed by a maximum at 975 Hz. Just as with the previous exploration of EOD frequency, the small shift in

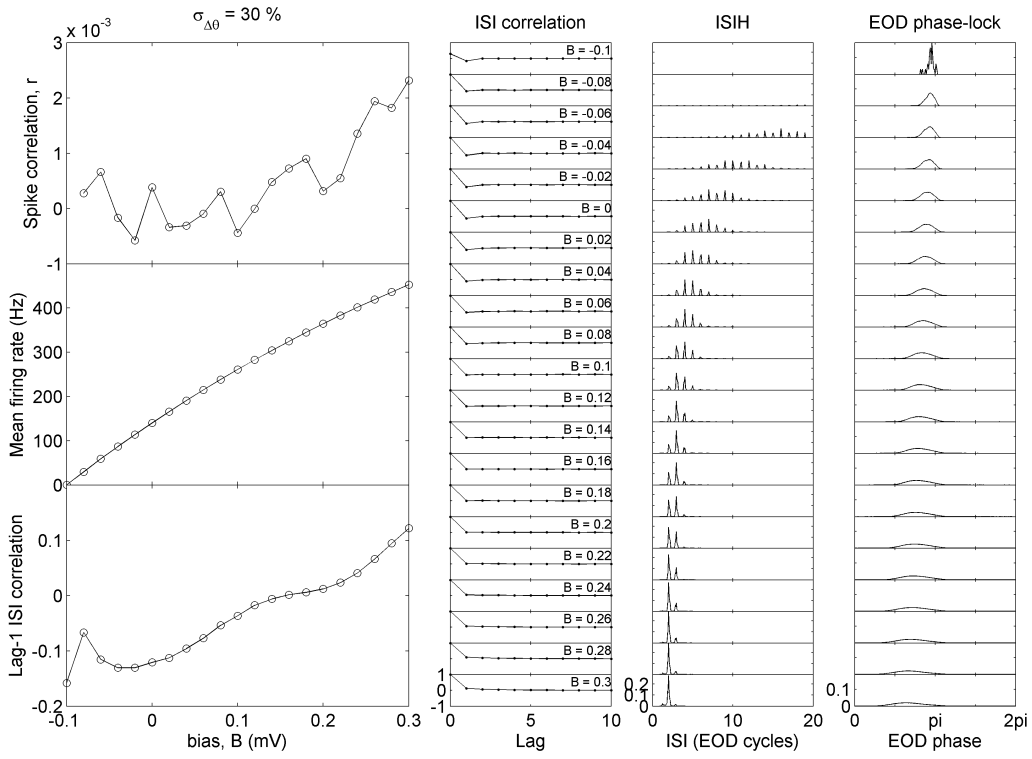


Figure 3.5: Baseline model statistics varying input bias $B$ (mV; standard value is 0 mV) at 30% threshold increment jitter ($\sigma_{\Delta\theta} = 0.3$). All other parameters as in Fig. 3.3.

the ISIHs is only due to the change in unit size since the mean firing rates differ by only 1.5%.

The 900-Hz EOD frequency is again a point of interest when analysing lag-1 ISI correlation, as a local minimum occurs at this value as a sharp kink in the curve; local maxima are located near 850 and 950 Hz similar to the extrema in mean firing rate. At higher lags, the ISI correlations are larger in this case than in any previous one implying much longer memory

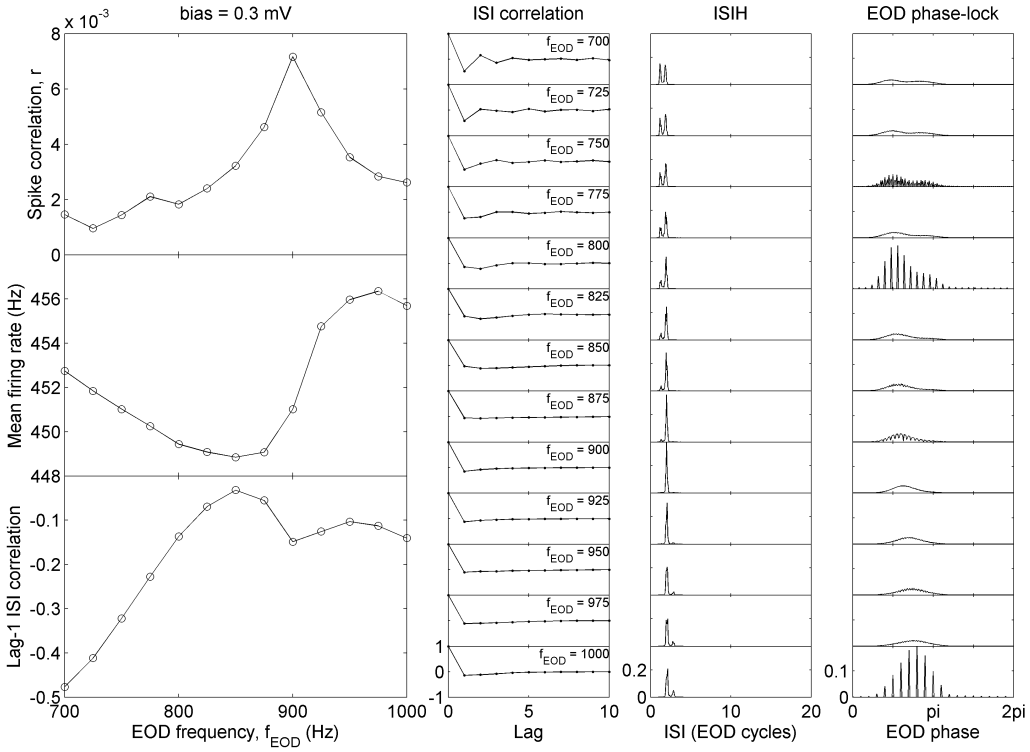


Figure 3.6: Baseline model statistics varying EOD frequency $f_{\mathrm{EOD}}$ (Hz; other figures in this section at 900 Hz) at high input bias ($B = 0.3$ mV). All other parameters as in Fig. 3.2.

in the system, hence a dependence on many more preceding ISI values than the accepted singular lag. At 700 Hz, for example, not only are adjacent ISIs negatively correlated, but those separated by another ISI between them are mildly positively correlated—that is, every *other* ISI will tend to have a similar length with respect to the mean. This pattern oscillates for several lags with diminishing strength and is indicative of fairly periodic behaviour.

The EOD phase-lock is just barely bimodal at the start of the frequency range showing two local maxima in the first few distributions. This bimodality dissipates around a frequency of 800 Hz as the second mode gradually turns into a long tail appended to the main distribution at about 850 Hz; this form is then reversed after a symmetrical distribution at 950 Hz. Furthermore, a resonance effect at 800 and 1000 Hz again produces discrete-looking distributions as in the zero-bias case (Figure 3.2) likely due to phase locking.

The maximum in the spike correlation, as well as the sharp dip in ISI correlation, that are seen at EOD frequency $f_{\mathrm{EOD}} = 900$ Hz appear to be associated with near-perfect periodic spiking with a firing rate (451 Hz) very near a subharmonic of this sinusoidal forcing frequency ($900/2 = 450$ Hz). This is visible in the ISI histogram as a single peak at 2 EOD cycles, meaning that the neuron fires very nearly at every second EOD cycle. This regularity

presumably underlies the higher spike correlation.

### 3.3.6 Varying Threshold Time Constant

The baseline model statistics for varying threshold time constant $\tau_\theta$ are shown in Figure 3.7. The time constants take on the relative values 30%, 40%, ..., 120% of the "standard" threshold time constant $\hat{\tau}_\theta = 14.5$ ms. The spike correlation is once again trend-free, as expected. However, the mean firing

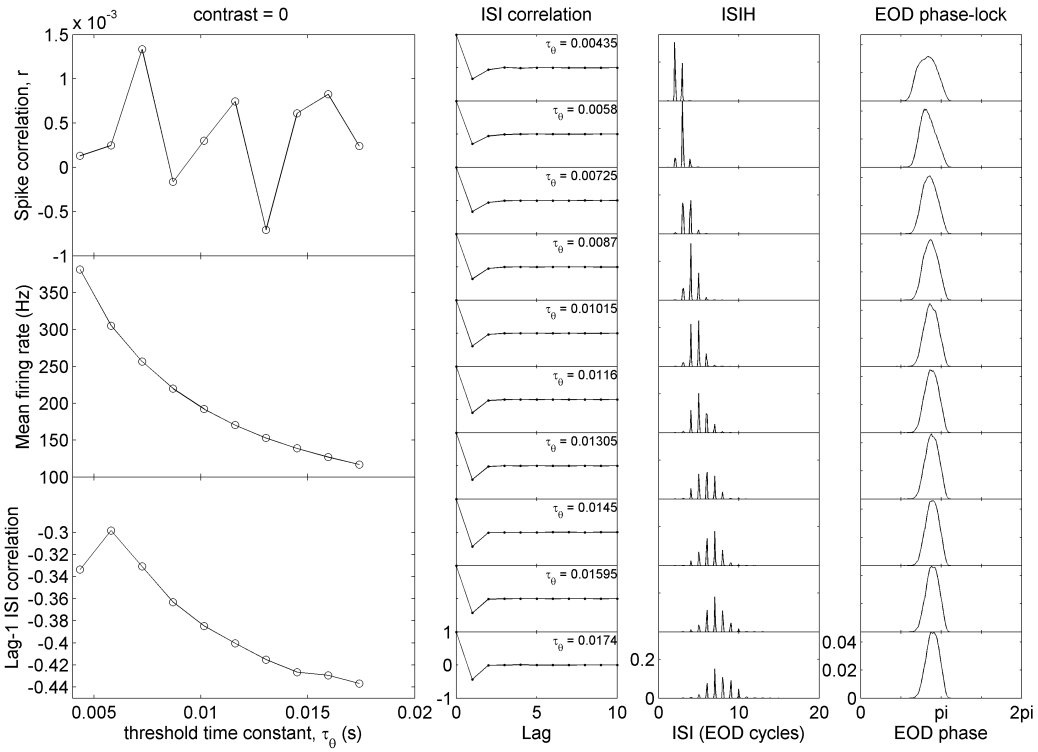


Figure 3.7: Baseline model statistics varying threshold time constant $\tau_\theta$ (s; standard value is 0.0145 s). All other parameters as in Fig. 3.3.

rate exhibits an inverse relation dropping from about 380 Hz down to about 120 over the domain of threshold time constants. This relationship is due to the fact that $\tau_\theta$ governs the decay rate of the dynamic threshold, dictating the amount of time it takes for the threshold to come back down after a spike to meet the membrane potential and produce the next spike. The larger the time constant, the slower the decay of the threshold, and the longer it takes for the potential to reach the threshold. With the exception of $\tau_\theta = 0.3\hat{\tau}_\theta = 0.00435$ s, the ISI correlations at lag one also have a decreasing trend as $\tau_\theta$ increases, varying from $-0.30$ to $-0.44$. These are all moderately strong negative correlations agreeable with the expected behaviour seen in experiment [14]. In addition, the correlations at longer lags are insignificantly different from zero for the full range of time constants, also in agreement with experiment. The EOD phase-lock shows a slight trend of decreasing variance in the distributions coupled with a mild increasing trend of the mean asymptotically approaching $\pi$.

### 3.3.7 Varying Threshold Increment

Continuing from the threshold time constant, Figure 3.8 explores the closely related parameter of threshold increment $\Delta\theta$ at 10%, 20%, ..., 160% of

the standard increment $\delta\theta = 0.05$ mV. There is again no trend in the spike correlation curve. Also, the mean firing rate curve shows a similar inverse relation to increasing threshold increment falling from about 640 to 100 Hz. However, the spread of the ISI histograms is larger when compared to similar firing rates for varying threshold time constant (Figure 3.7). There is an outlying lag-1 ISI correlation of about $-0.3$ at $\Delta\theta = 0.1\delta\theta = 0.005$ mV, while the next several values gradually decrease from $-0.1$ and approach

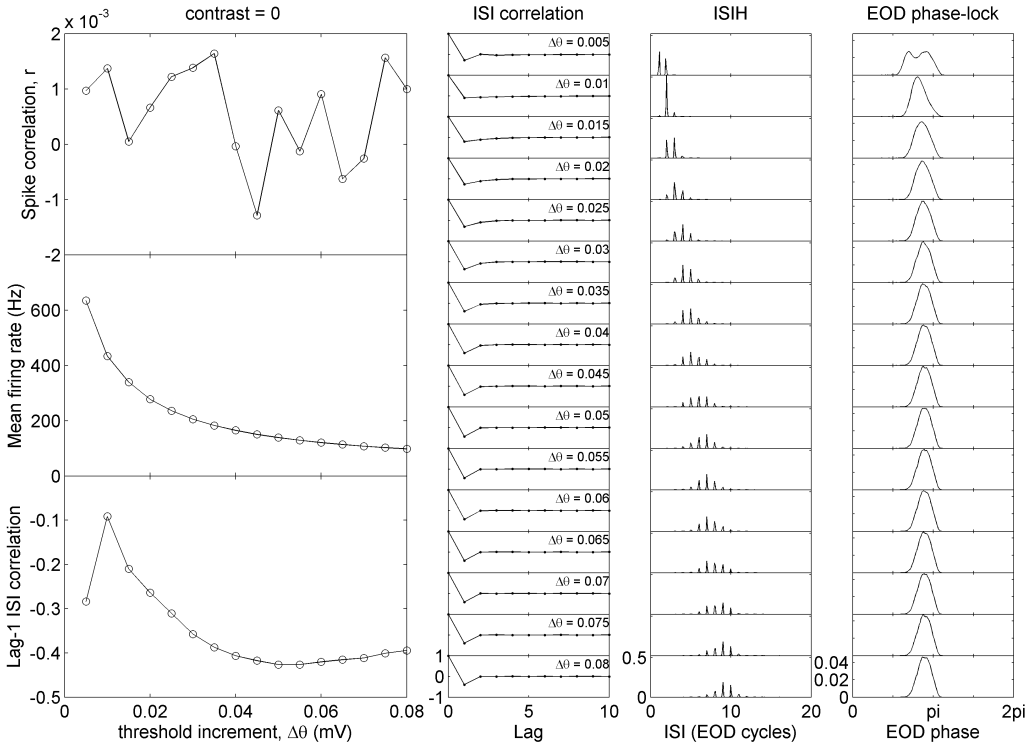


Figure 3.8: Baseline model statistics varying threshold increment $\Delta\theta$ (mV; standard value is 0.05 mV). All other parameters as in Fig. 3.3.

$-0.42$ at $\delta\theta$ and $1.1\delta\theta = 0.055$ mV before slowly climbing to $-0.39$ at $1.6\delta\theta$ $= 0.08$ mV. There are some mild deviations from zero for the first few lag-2 ISI correlations, but they diminish by about 80% of $\delta\theta$, that is, about 0.04 mV. A solitary bimodal EOD phase-lock distribution occurs at the already anomalous $0.1\delta\theta$ followed by a slightly skewed normal distribution and two wider-than-average distributions. Then, from 50% of $\delta\theta$ (0.025 mV) onwards the distributions change very little (with the exception of minor discretisation effects at some of the peaks).

### 3.3.8 Varying Threshold Increment with 30% Jitter

Figure 3.9 shows the results from repeating the exploration of the threshold increment, but with 30% jitter on the increment value. As seen before exploring bias space with increment jitter (Figures 3.4, 3.5), the main effect is to significantly reduce the magnitude of the ISI correlations as the shape of the lag-1 curve is similar to the case without jitter, although the minimum is about $-0.13$ at $\Delta\theta = 0.8\delta\theta = 0.04$ mV (excluding the once again anomalous reading at $0.1\delta\theta = 0.005$ mV). In fact, the correlation at 20% of $\delta\theta$ (0.01 mV) has risen so close to zero that it would be difficult to distinguish it from a random sequence of ISIs. A secondary effect involves flattening out, and

hence broadening, the ISI distributions (compare Figure 3.8), though the means have stayed the same since the mean firing rates have not changed. The EOD phase-lock is virtually identical to the previous case and the spike correlation is qualitatively equivalent.

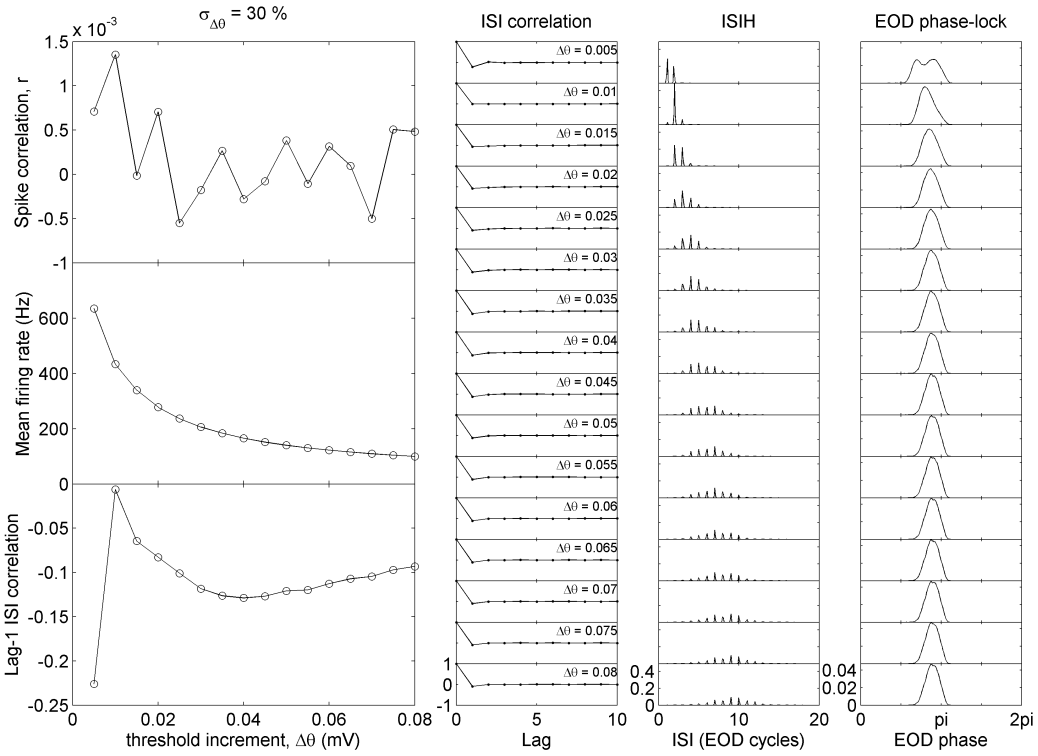


Figure 3.9: Baseline model statistics varying threshold increment $\Delta\theta$ (mV; standard value is 0.05 mV) with 30% jitter ($\sigma_{\Delta\theta} = 0.3$). All other parameters as in Fig. 3.3.

## 3.4 Synthesis of Input

Several types of signal are input to the neuron model examined in this study: the fish's unique, perpetual EOD signal; the beat produced when two such signals with differing frequencies overlap; the chirp that one of the fish produces to very briefly break up the beat signal in a specific way; and a random amplitude modulation simulating random obstacles encountered by the fish. Their implementations in the model are presented here to show some basic properties of the responses to these types of input.

### 3.4.1 EOD

The EOD is the basic signal in the P-unit model used as a carrier signal for all the other inputs. It is the underlying signal involved in all of the fish's interactions with its environment. Recordings of the electric field generated by *A. leptorhynchus* show a period of an approximate sine wave followed by a very brief null, or pause, before the subsequent sine wave. Since the second (negative) half of the period is truncated in the neuron due to rectification, a standard sinusoid was used in Equation 3.2 to simplify the model.

### 3.4.2 Beat

When a wave-type electric fish is in proximity to a second, their EOD signals will overlap and a beat will be created analogous to two sounds of similar pitch. Just as in the auditory case, the beat will have a frequency equal to the difference in frequencies of the two EODs, $\Delta f = |f_{\mathrm{EOD}_1} - f_{\mathrm{EOD}_2}|$, as introduced in Equation 3.2. If the two signals had equal contributions to the compound signal at the electroreceptors, say $A_0$, the contrast, or strength, of the amplitude modulation would be 100% as the maximum value of the superposition in each beat period would fall from $2A_0$ to zero and back. This would trace out an envelope shaped like the absolute value of a cosine with frequency $\Delta f/2$ and amplitude $2A_0$. The shape of the positive part of the envelope, which is of main concern in terms of what fires the electroreceptor, can be very roughly approximated by a standard cosine with amplitude $A_0$, vertically offset by $A_0$, and twice this frequency, namely $\Delta f$ (as promised). This approximation improves substantially as the two amplitudes become unbalanced, as so happens at the receptors where the electric field produced by the native fish is much stronger than that of the foreign fish. By the same token, the frequency of the carrier is better approximated by the native fish's EOD frequency. (The same trigonometric identity that dictates the former

behaviour—for equal amplitudes—also states that the carrier signal would have as frequency the average of the two individual frequencies.)

Figures 3.10 and 3.11 show the neuron model's response to various beats for the deterministic and stochastic cases, respectively. Shown in the left column are *raster plots* with a data marker at each spiketime within a sample time period arranged in rows for each of 20 realisations at a specific beat frequency. The beat envelopes (Equation 3.3) are superimposed in each plot, though the scale is 70–130% of $A_0$ (for 30% contrast). In the next three columns are the familiar ISI correlation, ISIH and EOD phase-lock plots from the preceding figures, as well as an extension of the phase-lock for the beat phase in the final column (however, this phase begins at the minimum of the envelope). The simulations explore 10- to 300-Hz beats (as labelled to the left of each row) modulating a 900-Hz EOD signal. (Although a 300-Hz beat would only be physically possible with one EOD at 700 Hz and the other at 1000 Hz for this species, which is possible in certain male-female interactions, this experiment is very informative in identifying patterns and predicting them for the general case.) A random value was chosen for each realisation for the initial membrane potential at the start of the simulation since it is reasonable to assume that the moment of stimulus onset is stochastic even

if the neuron's response is not (also the repeated realisations would provide no additional statistical information in the deterministic case as their runs would be identical).

For the deterministic model behaviour shown in Figure 3.10, several raster plots hint at chaotic-like behaviour in the sense that miniscule perturbations in the timing of a spike lead to significantly different evolutions of the model solution. Specifically, at beat frequencies of 30, 40, 100, 110, 170, 180, 190, 210, 240, 250, and 260 Hz the spiketimes of two or more realisations appear aligned or nearly so, but not all of them produce their next spike within the same EOD cycle, or even the same beat. However, the dynamic threshold must be considered as a second dimension, which may have large differences between realisations, corresponding to distant regions in phase space, breaking the similarity to chaos. In fact, the behaviour is quite regular and periodic as evidenced by the ISI correlations. Some are obvious, such as for $\Delta f \in \{70, 220\}$ (with a period of two ISIs) and $\Delta f \in \{150, 200, 250, 300\}$ (with a period of 3), and even $\Delta f \in \{210, 240\}$ (period-5) where a recognisable pattern repeats at the specified lag. However, closer examination of the ISIH as well as the EOD and beat phase-lock at 150 and 300 Hz reveals that the ISIs are essentially equal for their respective beat frequencies and the beat

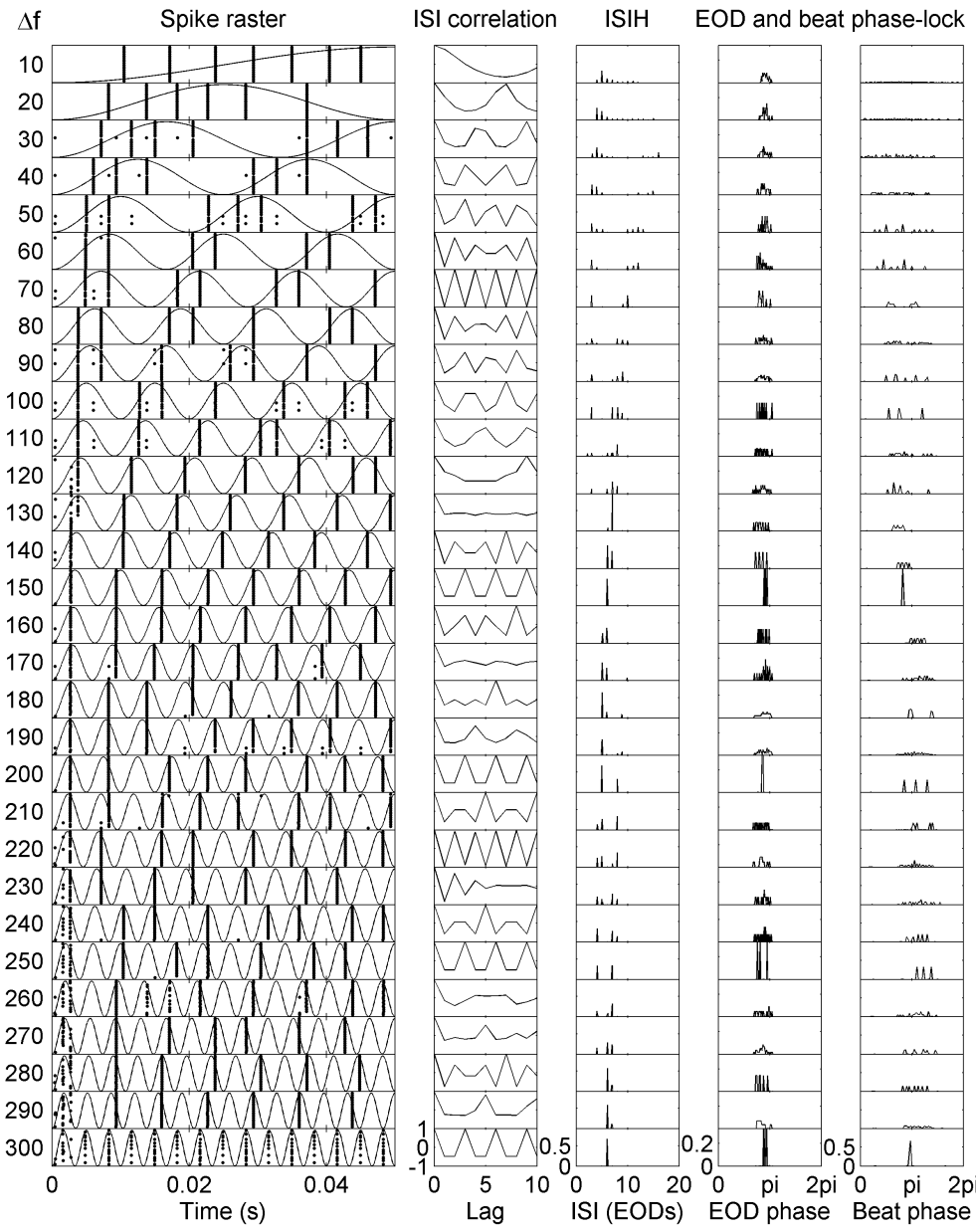


Figure 3.10: Spike rasters of P-unit model with no internal noise ($\sigma = 0$) for 30% beat stimulus with various beat frequencies $\Delta f$ (labelled on left in Hz). $f_{\mathrm{EOD}} = 900$ Hz. All other parameters as in Fig. 3.1.

phase at the time of a spike is virtually constant, whereas the EOD phase takes on three equally likely, extremely close but distinct values producing three extremely close but distinct ISIs. This appears to generate periodic behaviour with a period of three ISIs as interpreted from the correlations, when in essence there is only a single ISI. On the other hand, a true period of three ISIs occurs for 200 and 250 Hz where two truly distinct ISIs produce a pattern of two shorter ISIs followed by a longer one and two long ISIs followed by a short one, respectively, phase-locked to three distinct beat phases.

A similar examination at 220 Hz leads to a similar conclusion: an oscillation of period 2 cannot exist with four distinct ISIs; in fact, the correlations at lag 2, 4, and 6 are not quite perfect—this case has a true oscillation of period 8, since the correlation at lag 8 returns to a value of 1. This is another way to deduce the period of oscillation without explicitly observing a repeating pattern in the correlation. For $\Delta f = 20$ and 30 Hz, this condition is very nearly met at lags 7 and 9, respectively, but the correlation is slightly below 1 so the oscillation will only approximately be periodic with those periods. The following frequencies are more definitive: $\Delta f = 180$ Hz, $\Delta f \in \{100, 140, 280\}$ Hz, $\Delta f = 160$ Hz, $\Delta f = 120$ Hz, and $\Delta f = 40$ Hz with respective

periods of 6, 7, 8, 9, and 10.

Another attribute possessed by all correlation data sets is a symmetry of values centered at the mid-point between two perfect correlations. If a perfect correlation is not repeated in the given data set, then this symmetry can be exploited to infer the period as twice the value at the axis of symmetry. The following periods of oscillation can be inferred at the given beat frequencies: 11 at 60 Hz; 13 at 130 Hz; 14 at 50 and 110 Hz; 15 at 230 Hz; 16 at 170 Hz; and 18 just barely at 80 Hz. The remaining beat frequencies will have periods of repetition of at least 20 ISIs. Furthermore, beats of 130 and 170 Hz produce the smallest correlation values resembling correlation plots of random ISI sequences (even though their raster plots show otherwise).

Comparing the responses of the noisy model shown in Figure 3.11 to those of the deterministic model, there is much more variability in the outputs and statistics as seen by the decrease of synchronisation between the neurons in the spike rasters and by the larger spreads in the distributions of ISIs and EOD and beat phase-lock. However, most of the means and modes change very little; although, one counterexample is at a beat frequency of 150 Hz where the model also locks in to a second favourable beat phase.

The ISI correlations for beat frequencies of 140 Hz and above are similar

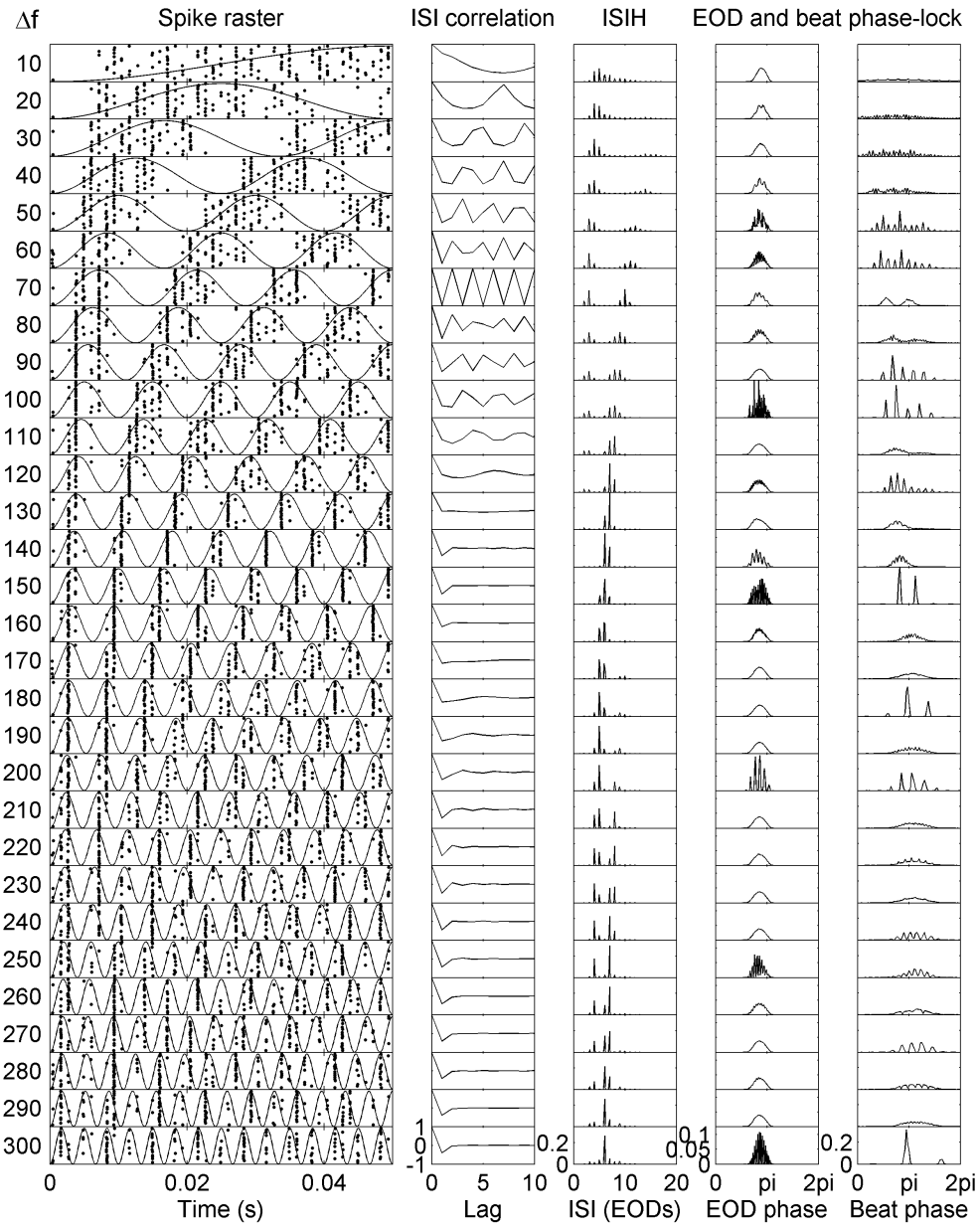


Figure 3.11: Spike rasters of P-unit model with internal noise intensity $\sigma = 0.002$ for 30% beat stimulus with various beat frequencies $\Delta f$ (labelled on left in Hz). All other parameters as in Fig. 3.10.

to those for baseline activity showing negative correlations at lag 1 and no memory thereafter. Conversely, for beats of up to 110 Hz the patterns are very similar to those previously shown for the model with no noise. Although the values are generally smaller in magnitude, there is a high degree of memory at large lags, especially at 70 Hz with near-perfect repetition of ISIs with period 2. Also echoing the results of the noiseless system, the simulations at 130 Hz show no memory at any lag, defining an imaginary boundary between the two regimes for multi- and single-lag memory.

### 3.4.3 Chirps

A chirp was described earlier as a "brief frequency excursion" where one of the two interacting fish will momentarily alter the rate of the discharges from its electric organ in order to disrupt the beat signal generated by their combined EOD signals. One type of chirp will effectively advance the phase of the beat very rapidly—this is called a *small chirp*. The other type is a *big chirp* (also called a *large chirp*), which is longer in duration than the small chirp, and typically involves a large decrease in beat contrast for its duration. Instead of modifying the EOD frequency of the model to disrupt the beat, it is presumed that the fish with which the model is interacting produces a

chirp in order to observe the effects in the simplest case.

To produce the phase skip in the beat signal, a small bump is modelled for the phase velocity as a narrow Gaussian curve centered around the time of the chirp offset by the normally constant velocity. Integrating yields a continuous "step" in what would normally be a straight line representing the constant rate of increase of the beat phase. This new phase function is substituted for the sine argument in the definition of the beat modulation $\beta(t)$ in Equation 3.2. The duration of the chirp, and hence the width of the Gaussian curve, is determined from typical values observed in experiments.

Figure 3.12 shows the model's response to two examples of a small chirp occuring at opposite extremes of the beat signal: in the left column of plots the chirp is produced at the minimum, or trough, of the modulation resulting in a steep incline in amplitude, or *upstroke*, in the input signal as the beat phase is rapidly advanced to its maximal value (as illustrated in the top-left plot); in the right column the chirp accelerates the decline, or *downstroke*, from its peak into a trough (top-right plot).

The next row shows raster plots of spiking events for 20 realisations of the neuron model with dynamic threshold for the two cases. A higher-than-average concentration of events can be identified by visual inspection at the

upstroke while a unanimous absence of activity is observed at the downstroke. This visual deduction is affirmed in the following plots of instantaneous firing rates averaged over all realisations: a sharp peak of about 300 Hz occurs at the upstroking chirp, where normally the maximum reached is about 200 Hz; in the downstroke case a low trough with steep walls is observed with a minimum near 50 Hz while the normal minima stay above 75 Hz. The same

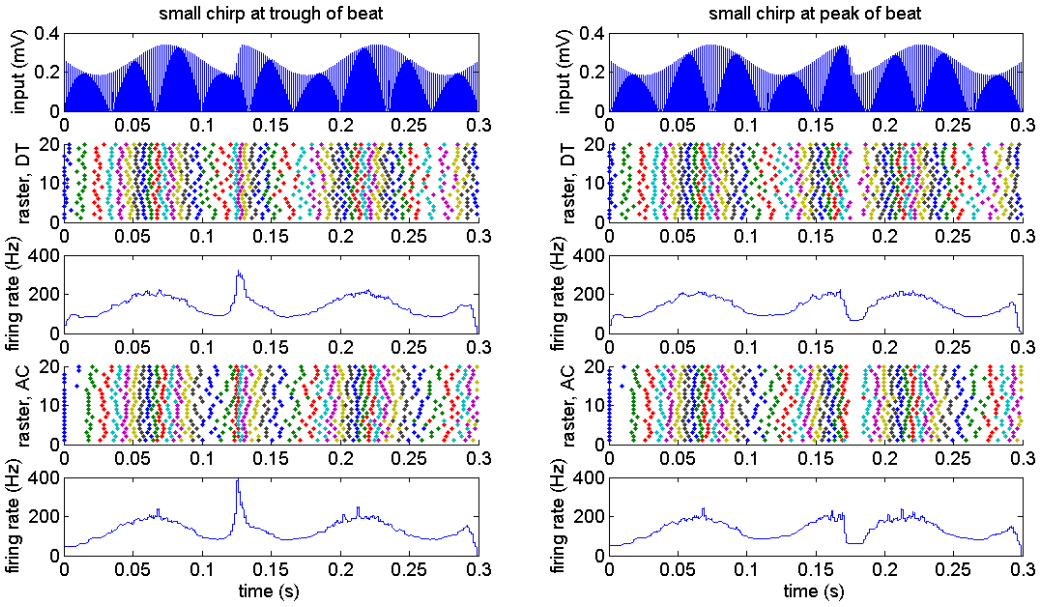


Figure 3.12: An EOD signal modulated 30% by a 10-Hz beat with a small chirp (top row) produces a spike raster by the stochastic P-unit model with dynamic threshold (second row) and adaptation current (fourth row) showing, in their respective plots of instantaneous firing rate (third and bottom rows), an increase in spiking activity during a rapid upstroke in the beat (left column) and a decrease therein (or lack thereof) during a rapid downstroke (right column). (Compare with [3], Fig. 3; [4], Fig. 7.)

set of plots is shown below for the same experiment simulated with the model implementing the adaptation current instead. The results are qualitatively alike, but with a noticeably larger effect from the upstroke as firing rates peak near 400 Hz.

### 3.4.4 Gaussian Noise

To generate a random amplitude modulation (RAM) of the EOD signal simulating obstacles encountered by the fish in a natural environment, a sequence of Gaussian random variates was subjected to zero-phase forward and reverse digital filtering of Zero-Pole-Gain design, implementing a second-order sections form of a narrowband Butterworth filter with a passband of 40–60 Hz. This signal is then normalised to have the desired standard deviation (or contrast). The envelope of this signal is also extracted by calculating the magnitude of the analytic signal of the RAM (Equation 2.5) via the Hilbert transform (Equation 2.6). Figure 3.13 shows a sample RAM signal $S$ and its envelope $E$ in the time and frequency domains. Since $E$ is a nonlinear transformation of $S$, its spectral density shows power at 0–20 Hz because of the 20-Hz range of the passband of $S$.

Figure $\pi$ shows the response of the P-unit model to a RAM signal. A

sample of the original signal $S(t)$ is shown in the top panel; its envelope $E(t)$ is below. Next is the overall input signal $I(t)$ (EOD signal modulated by $S(t)$). A spike raster for 20 realisations of the model follows, with a sample spike train from a single realisation. The bottom panel shows the ISI histogram from all spikes in all realisations.

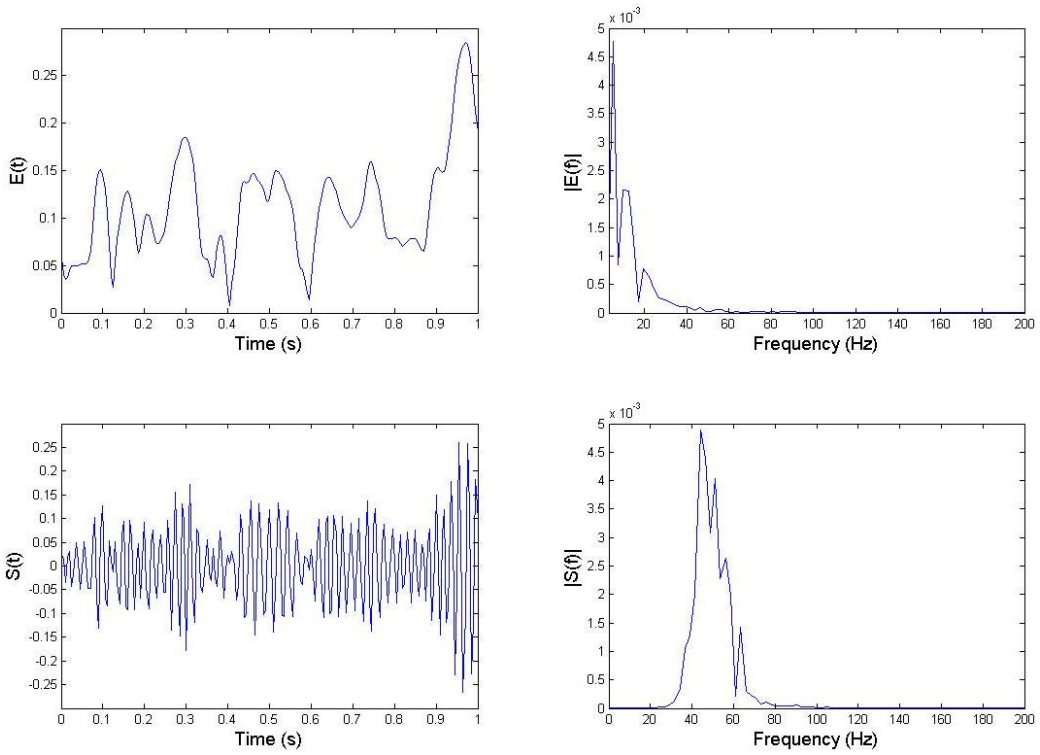


Figure 3.13: Narrowband stimulus $S(t)$ (bottom row) in the range 40–60 Hz from a filtered Gaussian noise signal and its envelope $E(t)$ (top row) showing power in the range 0–20 Hz in its spectral density on the right.

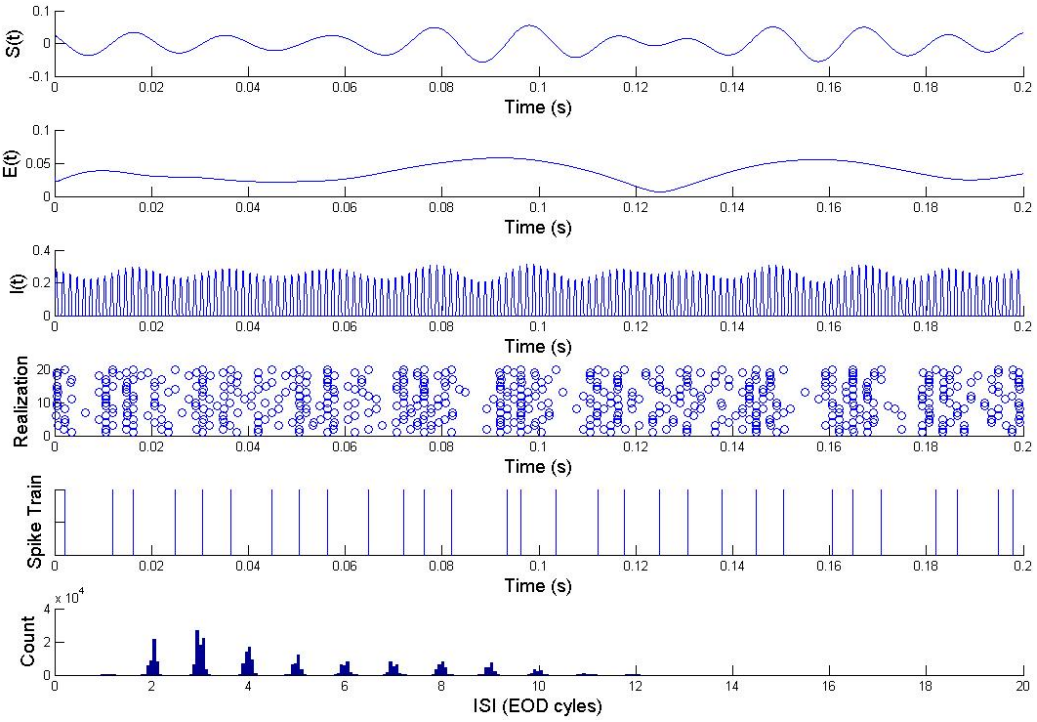


Figure $\pi$: (From top to bottom) RAM stimulus $S(t)$ from filtered Gaussian white noise with a passband of 40–60 Hz and 15% contrast, its extracted envelope $E(t)$ and the resultant input signal $I(t)$ showing modulated EOD signal. Below, a spike raster for 20 independent realisations of the P-unit model, as well as a sample spike train from one realisation and the ISIH obtained from firing events across all realisations.

# Chapter 4

# Linear vs. Nonlinear Encoding

Portions of the material in this chapter were published by Longtin, Middleton, Cieniak, and Maler in 2008 [18].

As mentioned previously, the coherence measure of the P-unit model response to the RAM signals can be used to describe the level of nonlinearity in the translation, or *coding*, of the input signal into the output spike train. This level can be determined by the coherence of the response in relation to the nonlinear envelope extracted from the stimulus via the Hilbert transform—the higher the coherence to a nonlinear signal, the higher the nonlinearity of the model's encoding scheme.

The extent of linearity of the model can also be inferred from its $f$-$I$ curve and the nature of the stimulus. As shown in Figure 2.2, the basic $f$-$I$ curve for a model with no noise has non-zero firing rates only for signal

intensities above a certain threshold. Up to this threshold, the curve is a straight line of all zeros, then starts increasing suddenly creating a kink in the graph (a nonlinear characteristic). If the stimulus is designed in such a way as to explore this region of the model by including the critical intensity in its range of amplitude modulation, then the model is expected to behave nonlinearly. To avoid this regime, either the $f$-$I$ curve can be made less nonlinear by increasing the noise and rounding out the kink or the kink can be avoided altogether by either increasing the input bias or reducing the stimulus contrast so the critical intensity is not included in the modulation range of the signal amplitude.

## 4.1 Linearisation with Noise

The effect of the first option on the coherence measure is shown in Figure 4.1. Figures 4.1A and C on the left show statistics for a model with high noise while Figures 4.1B and D on the right show data for a model with low noise. Both models show the same high level of coherence between the stimulus and the response, $C_{\mathrm{SR}}$, in the top subfigures (4.1A and B), where the level is generally above 0.9 in the same frequency range as that of the

RAM (40–60 Hz). However, only the low-noise model records significantly different envelope-response coherence, $C_{\mathrm{ER}}$, in the envelope frequency range of 0–20 Hz as shown in Figure 4.1D by the steady increase in coherence from about 0.1 to about 0.7 for decreasing frequency from 20 to 0 Hz (compare with relatively flat curve in Figure 4.1C).

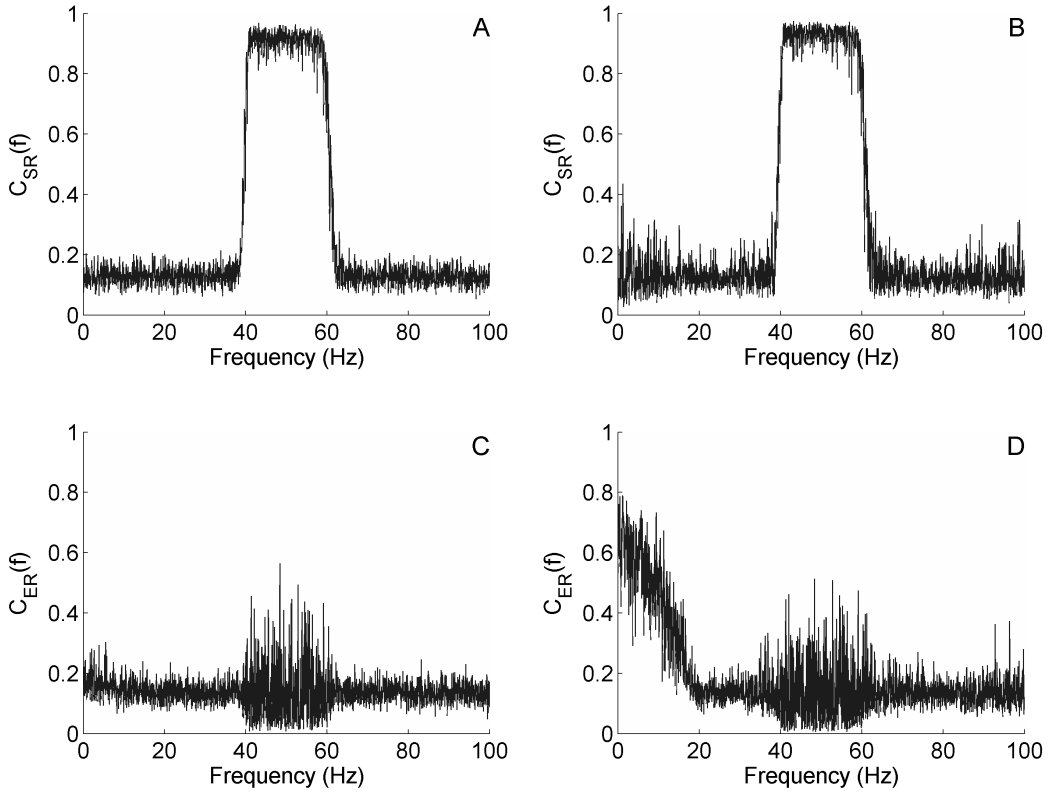


Figure 4.1: (A,C) Linear (high noise) and (B,D) nonlinear (low noise) P-unit model response coherence to (A,B) narrowband filtered Gaussian noise stimulus in the range 40–60 Hz and (C,D) its 0–20-Hz (nonlinear) envelope [18]. (Reproduced with permission.)

## 4.2 Linearisation with Bias

The effect of the second option is shown in Figure 4.2. Instead of a larger noise parameter, the model now incorporates an input signal with bias $B = 0.2613$ mV—equal to the EOD amplitude $A_0$—putting the signal well above the firing threshold and away from the nonlinearity in the $f$-$I$ curve. Just as in the high-noise case above, the model response shows both excellent coherence

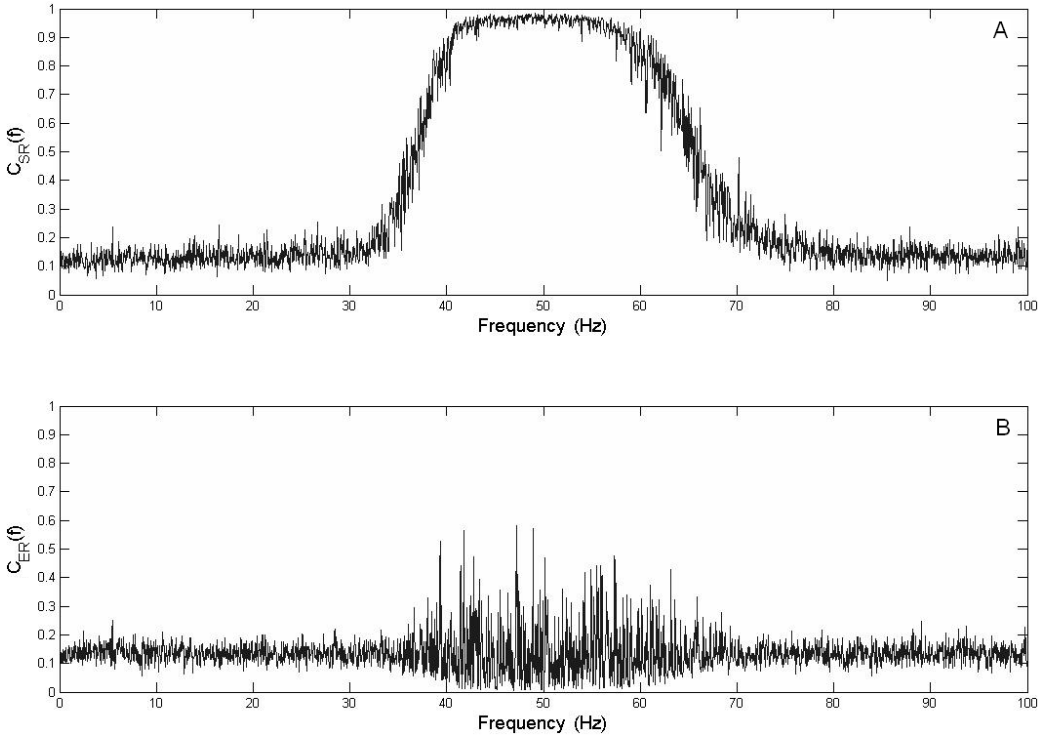


Figure 4.2: P-unit model with high input bias ($B = 0.2613$ mV) response coherence to (A) narrowband filtered Gaussian noise stimulus in the range 40–60 Hz and (B) its 0–20-Hz (nonlinear) envelope.

to the stimulus in the 40–60-Hz range (0.95, Figure 4.2A) and poor coherence to its envelope in the 0–20-Hz range (0.15, Figure 4.2B).

# Chapter 5

# Response to Communication Signals

The beat signal produced by the interference of the EOD signals of two nearby knifefish is a *passive* form of communication between the fish (as they do not proactively alter their signals to generate the beat, in contrast with the production of chirps). Nevertheless, information about the other fish is decoded from the response of the electroreceptors encoding that information in their spiking activity and the synchronisation thereof between multiple cells. This chapter investigates whether the synchrony seen experimentally [4] can be simulated by the model presented in this work, and thus give a better understanding of its origins.

## 5.1 Response to Beats in Simulation

The behaviour of the simulated neurons when presented with a beat stimulus depends strongly on the frequency of the beat, as previously seen (Figure 3.11). The frequency also determines the level of synchrony between similar neurons, that is, ones with identical model parameters but different sequences of random variates creating the internal noise. Certain values of the frequency even produce a type of "resonance" effect causing very highly synchronous firing patterns across a small window of values within the frequency domain. This level of synchrony will now be quantified with the spike correlation measure as a function of the beat frequency. The effects of varying certain model parameters on the synchrony are presented below.

### 5.1.1 Varying Internal Noise

Figure 5.1 displays plots of several statistical measures showing the effect of internal noise $\sigma$ on the response of the neuron model. On the left are plots of the spike correlation and mean firing rate as functions of the beat frequency with separate curves for each noise value, ranging from 0 to 0.008 every 0.002.

It may not be surprising at first that the spike correlation is perfect in the

deterministic model without noise for over two-thirds of the beat frequency values and above 0.85 for all but one of them. However, considering that each realisation began with the membrane potential initialised to a random value, this is not a trivial result. The apparently anomalous drop of spike correlation to nearly 0 at 300 Hz is an artifact of the randomly prepared neurons forming two synchronised groups of approximately equal sizes that are 180° out of phase (see Figure 3.10, bottom row). When noise is introduced into the

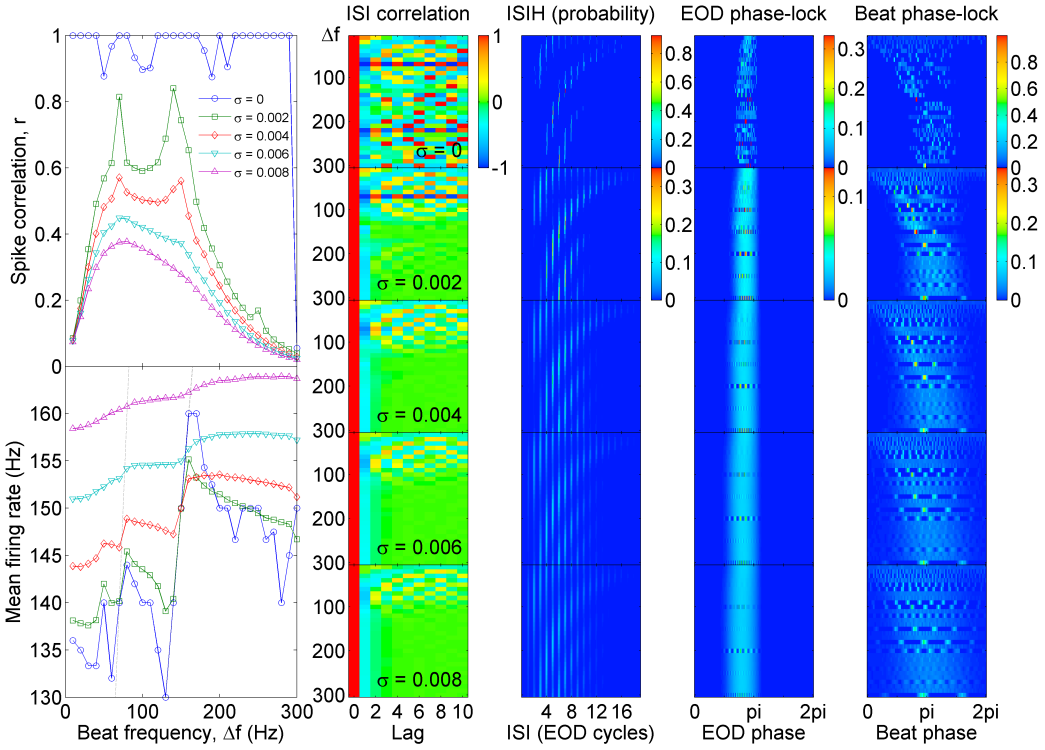


Figure 5.1: Analysis of the P-unit model response to beat signals (Eqs. 3.1–3.3) across a range of frequencies for various noise intensities $\sigma$. All other parameters as in Fig. 3.11. Layout described in body text.

system with the stochastic model, the spike correlation drops but remains moderately high for a broad range of beats. The curve has an underlying shape that resembles a skewed Gaussian curve or an alpha function with generally higher values at lower frequencies. This shape is close to that measured on experimental data [4]. However, the more noticeable features of the curves are the resonance peaks protruding out of the underlying shape at specific frequencies; at these frequencies the spike correlation is higher than would be expected from the correlations at nearby frequencies. Two prominent peaks are located around beats of 70 and 140 Hz for a noise parameter of 0.002 with values reaching above 0.8, exceeding the values of around 0.6 at their bases by about 30%. As the noise intensity increases, not only does spike correlation decrease significantly—by nearly one-half at $\sigma = 0.008$—so do the relative sizes of the resonance peaks, down to about 10% at $\sigma = 0.004$ with peaks of about 0.55 poking above a base of 0.5, then nearly completely eroded away to barely discernible bumps at $\sigma = 0.006$, until no trace of them is left by $\sigma = 0.008$.

Another effect of bringing the noise into the system is a tendency to slightly increase the mean firing rate by a few hertz for each increase of 0.002 in the noise parameter. Also, the stochastic-like variation in the curves is

smoothed out as noise increases and the overall range of firing rates over the beat frequency domain decreases substantially from 30 Hz at $\sigma = 0$ to 5 Hz at $\sigma = 0.008$. Interestingly, the curves of the mean firing rates suggest that the neurons adjust their spiking pattern to resonate with the beat frequency, or its harmonics. This is shown by straight dotted lines indicating where the firing rate is equal to an integral multiple of the beat—however, it is probably more informative, and accurate, to say that they are forced into this resonant state by the driving input. It is this periodic forcing that synchronises neurons with intrinsic firing rates near harmonics, and possibly subharmonics, of the beat frequency; it is the source of this resonance-induced synchrony enhancement (or RISE). The frequency domain over which the neurons resonate with the beat corresponds to the domain of frequencies for which the mean firing rate is near a harmonic of the beat frequency; in other words, the more frequencies there are at which the firing rate curve follows the harmonic lines, the wider the resonance peaks will be.

The remaining columns of subfigures respectively display data for ISI correlation and histograms for ISIs as well as EOD and beat phase-lock. In fact, these are the same statistics shown when introducing the beat stimulus previously, except with the beat frequency values compressed into the vertical

axes of smaller figures and the original vertical axes (ISI correlation and probabilities) rotated perpendicular to the page with values indicated by colourmaps (either shown to the right of the plot or using the same one from the plot above otherwise). The stacked subplots now differ in the value of another parameter indicated within the ISI correlation plot for each row of figures (in this case, the noise $\sigma$). This layout allows for quick identification of patterns in a very large amount of data by visual inspection.

Beginning with the ISI correlation, an intriguing pattern of concentric rings of alternating positive and negative values is visible in the plot for the deterministic model centered at a lag of 7 and $\Delta f$ of 70 Hz. This is due to the decreasing periods (and quasi-periods) of oscillatory behaviour in the ISI correlation curves, discussed earlier, as the beat approaches 70 Hz, after which they increase again. This pattern is broken up after the flat correlation curve at 130 Hz and looks scrambled, until after the next relatively flat curve at 170 Hz when this same pattern, though slightly compressed, appears between 180 and 250 Hz. With increasing noise values in the next panels below, the colours fade as the peaks recede from the extremes, but the pattern lingers with significant values away from zero for beats with frequencies up to about 100 Hz. Furthermore, the oscillating pattern of lag-1

correlations dampens as noise increases, levelling out at moderately negative values across most of the frequency range, except at 30 Hz and lower, with a minimum consistently occurring near 70 Hz. In the remaining three columns of plots, a trend of increasing data spread with increasing noise is universal, indicated by the "haziness" and fading of the colours.

This fading is also true of the EOD phase-lock for a fixed noise value (within one panel) as the beat frequency increases. However, the opposite is true of the beat phase-lock, whose spread decreases with increasing beat frequency, since the chance of firing early in the beat diminishes for faster beats. Also in the last two columns, the more "discrete", or multi-modal, phase-lock patterns at certain beat frequencies are quite noticeable—and very consistent across the range of noise values.

### 5.1.2 Varying Stimulus Contrast

Figure 5.2 shows the spike correlation and mean firing rate of the P-unit model response to beat signals (Equation 3.3) as the signal strength, or contrast $c$, is varied. The results for three values of contrast are examined: 10, 20, and 30%. As the contrast decreases, so does spike correlation, consistently across the entire beat frequency domain. What is not consistent across all

frequencies is the amount by which the correlation decreases. Specifically, the correlations at the resonance peaks do not decrease by as much as the rest of the curve, thereby resulting in an increase of the peak sizes relative to the underlying correlation curve for decreasing stimulus contrast. The relative peak sizes measured from their approximate bases on the underlying curves are about 30, 60, and 100% of the base value at 70 Hz and about 40, 70, and 200% at 140 Hz.

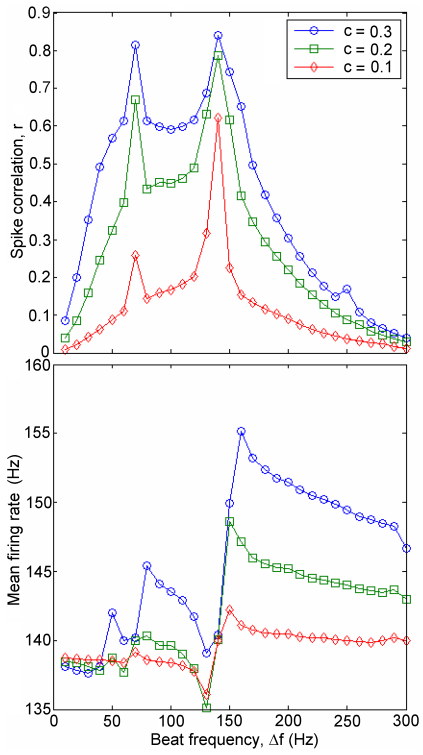


Figure 5.2: Spike correlation and mean firing rate as functions of beat frequency varying stimulus contrast $c$. All other parameters as in Fig. 3.11.

Reducing the strength of the signal reduces the overall synchrony of the model as it is driven less strongly by the input, reducing phase-locking. But, because the phase-locking is so strong when the beat harmonics are close to the natural firing rate of the neurons, they are able to resonate and retain high levels of synchrony.

### 5.1.3 Varying Bias

The effect of the input bias on the P-unit response, and in particular on the resonances, is shown in Figure 5.3. The plots of spike correlation and mean firing rate are now separated for each parameter value to reveal the relation of the peaks to the beat harmonics more easily. As the bias increases from 0 to 0.26 mV, the mean firing rate also increases, as expected from the baseline studies (Figure 3.3, for example; note the changing scale in the left-most figures). This significantly shifts the intersections of the firing rate curve and the dotted lines indicating harmonics of the beat frequency. Note also that the peaks in correlation (in the upper panel for each bias), marked by red vertical lines, faithfully line up with these intersections. Moreover, as the peaks move towards higher beat frequencies, their relative sizes tend to decrease in general compared to the underlying correlation curve, which also

gradually decreases by about one-half over the range of bias values.

### 5.1.4 Varying Threshold Time Constant

Figure 5.4 shows the effect on spike correlation and mean firing rate as the

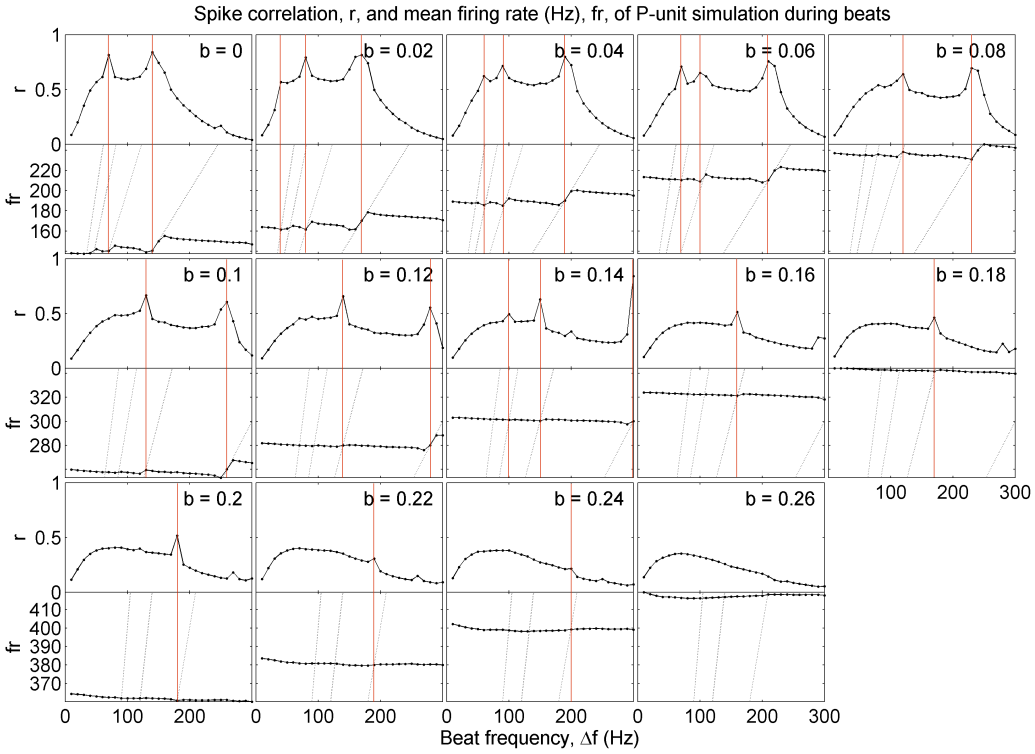


Figure 5.3: Spike correlation $r$ (top panel in each grouping) and mean firing rate $fr$ (bottom panel in each grouping) as functions of beat frequency varying input bias $b$ (mV; marked in each grouping). Dashed lines show firing rates equal to integer multiples of the beat frequency (1–4 from right to left; bottom row 2–4) and vertical lines highlight where a P-unit locks its firing (resonates) with the beat, shown by a nearby peak in spike correlation. All other parameters as in Fig. 3.11.

time constant $\tau_\theta$ of the dynamic threshold is varied from 80 to 120% of the standard value, $\hat{\tau}_\theta = 14.5$ ms. The same relation between peak location and firing rate results, only this time the firing rate decreases with increasing threshold time constant as expected.

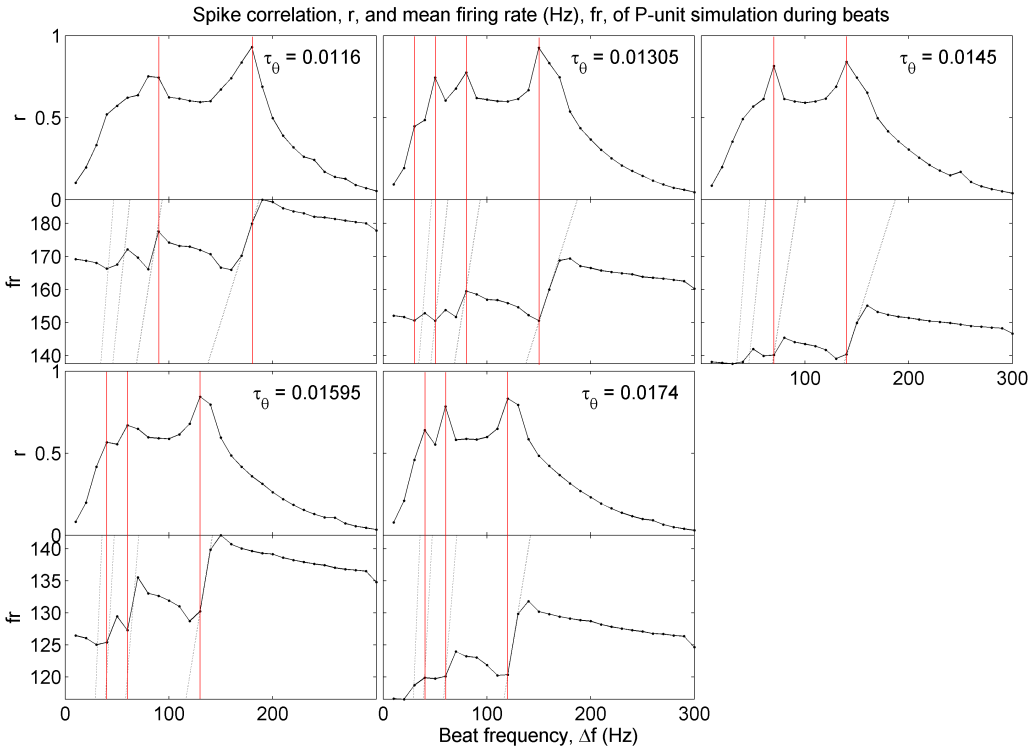


Figure 5.4: Spike correlation $r$ and mean firing rate $fr$ as functions of beat frequency varying threshold time constant $\tau_\theta$ (s). All other parameters as in Fig. 3.11. Layout as in Fig. 5.3.

### 5.1.5 Varying Threshold Increment Variability

Figure 5.5 shows how spike correlation and mean firing rate are affected by introducing various levels of threshold increment variability, or jitter, $\sigma_{\Delta\theta}$. As the increment jitter increases from 0 to 25% of the standard threshold increment $\delta\theta = 0.05$ mV, the sizes of the resonance peaks are significantly reduced, demonstrating that the RISE effect can be inhibited in the model.

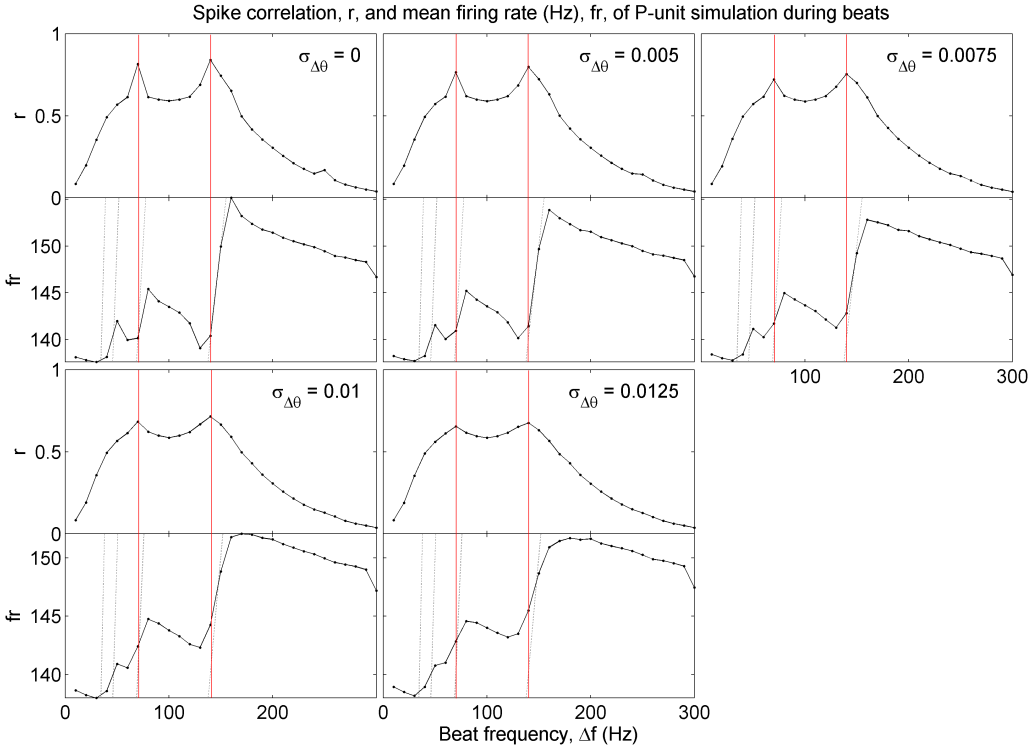


Figure 5.5: Spike correlation $r$ and mean firing rate $fr$ as functions of beat frequency varying threshold increment variability $\sigma_{\Delta\theta}$ (mV). All other parameters as in Fig. 3.11. Layout as in Fig. 5.3.

The rest of the correlation curve remains unchanged, as does the shape of the firing rate curves, although the range of the latter decreases marginally by about 3 Hz (2%).

## 5.2 Response to Beats in Experiment

The results of experimental P-unit recordings while stimulating with a beat signal are shown in Figure 5.6. The data are a subset of those used to generate the median values populating the spike correlation graph in Figure 1.1. The responses vary greatly between unique cells, but there are similarities to the simulated results, though some may be more subtle than others. Firstly, all of the neurons produce the same underlying shape in the spike correlation curves as observed from the model: a rapid increase in correlation values with a maximum at a beat frequency near 100 Hz followed by a gradual decline for the next 200 Hz, yielding generally higher values in the lower half of the frequency domain. This result is explored in detail in the literature [4]. Secondly, most firing rates that are approximately equal to a harmonic of the beat frequency correspond with a peak in the spike correlation at or near that beat frequency, demonstrating that the RISE effect exists in the real

P-units. This novel result was "hidden" in Figure 1.1 as the median values are unaffected by the peaks due to the high variability in their locations. The most illustrative examples include cells numbered 1, 2, 5, 6, 7, 10, 11, and 12. Neurons #3, 4, 8, and 15 provide more subtle examples. Few counterexamples are evident, at least at lower harmonics, though some possible ones are represented by cells #9, 13, and 14, where peaks fail to be produced

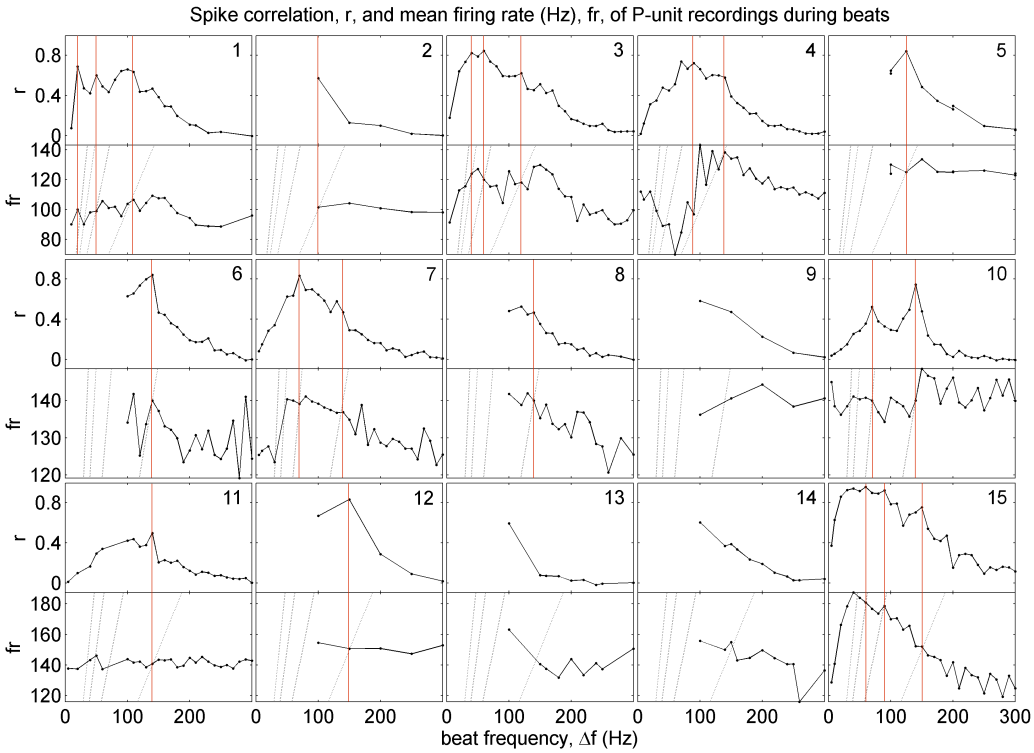


Figure 5.6: Spike correlation $r$ and mean firing rate $fr$ as functions of beat frequency for P-units recorded experimentally. Data provided by Jan Benda and collected in Prof. Maler's lab at the University of Ottawa. Each pairing of top and bottom panels represents a different P-unit. Layout as in Fig. 5.3.

in the correlation curves near firing rate crossings of the beat harmonics, or an apparent peak where there is no crossing (#13). Lastly, there is a very good correspondence between peak width and number of consecutive firing rate points that follow the harmonic lines very closely. Cells #1, 6, and 10 have very good examples of wide peaks, while most of the others have good examples of single-point peaks.

## 5.3 Response to Chirps

It is known that big chirps desynchronise P-unit firing patterns [4]. The effect of introducing a big chirp into a beat signal stimulating the model was examined to determine whether it can explain these findings. Separate analyses can be performed on the beat and chirp by separating the data into three regions: before, during, and after the chirp. The data before and after the chirp are then combined and compared to the data during the chirp. Figure 5.7 shows these results for a big chirp at various EOD amplitudes for both implementations of adaptation: dynamic threshold (DT) and adaptation current (AC). The chosen amplitudes $A_0$ were 0.05, 0.10, 0.15, 0.20, and 0.2613 mV (the latter being the standard value). The figure

shows consistently lower correlations during the chirps than the rest of the stimulus for both P-unit models at $A_0 = 0.10$ mV and above. These results are in agreement with experimental results, which also show a decrease in correlation during the chirps [4].

Furthermore, the lack of data at the lowest amplitude in the chirp cases is also significant. The amplitude is high enough to produce minimal spiking activity during the beat stimulus, hence the low correlation value. During

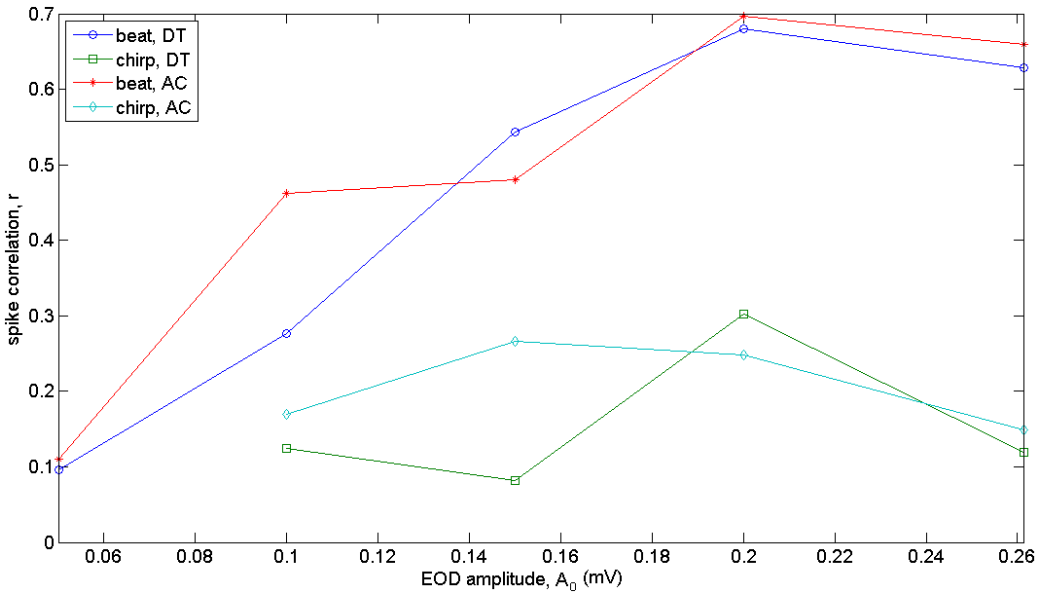


Figure 5.7: Spike correlation $r$ of P-unit model response to a big chirp at various EOD amplitudes $A_0$. Data are computed separately for the periods before, during, and after the chirp and then combined for the periods before and after, which contain only beats. Data for both dynamic threshold (DT) and adaptation current (AC) implementations are shown. All other parameters as in Fig. 3.11.

the chirp, however, all activity ceases and no spikes are recorded, therefore no correlation value can be computed over the duration of the chirp. This last outcome has been confirmed by other preliminary experimental results: Figure 5.8 shows the responses of real neurons to the same type of stimulation involving a big chirp. According to the spike raster in the top subfigure, these neurons also cease firing during the chirp, which is in qualitative agreement with the simulated results.

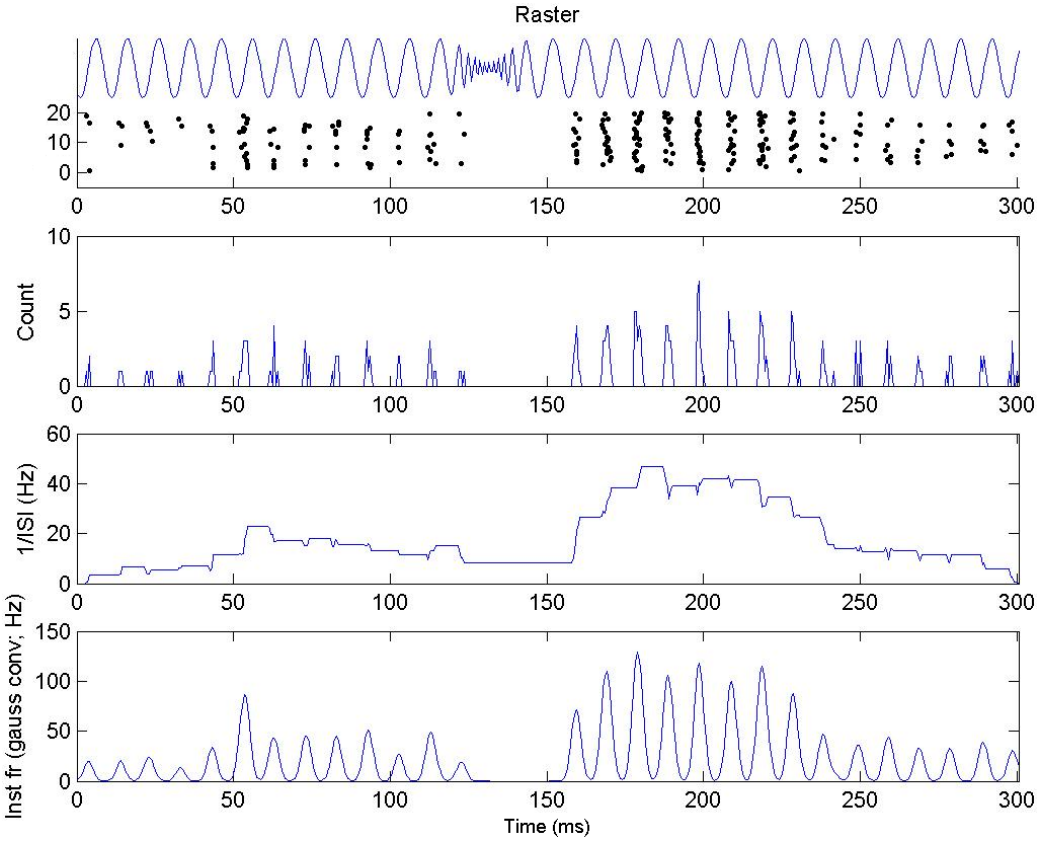


Figure 5.8: Responses to a big chirp from P-units recorded experimentally. Figure provided by Gary Marsat from data collected in Prof. Maler's lab at the University of Ottawa. The stimulus is illustrated in the top panel above the spike raster, which shows spike times for 20 trials. Following below are a spike histogram as well as instantaneous firing rate computed from the inverse of interspike intervals (1/ISI) and a Gaussian convolution of the spike trains (bottom figure).

# Chapter 6

# Discussion

The purpose of this work was to advance the development of a mathematical neuron model to reproduce and help explain the most recent experimental observations of the behaviour of the electroreceptor afferents of the weakly electric fish *A. leptorhynchus*, the brown ghost knifefish. The rationale behind the methodology of this study, the agreement of the results with experimental findings, as well as their implications are discussed below. Areas of further study for enhancement or validation of the model are also suggested.

## 6.1 Generating Neuronal Diversity

Being able to simulate a wide range of tuberous-type "P-unit" electroreceptors encountered in experimental studies, and to understand how their firing activities become correlated in the presence of specific natural stimuli,

provided the motivation for the exploration of the model parameter spaces. Testing the model with EOD frequencies across the entire natural domain of the brown ghost (Figure 3.2) validated that the model is well-behaved when simulating any member of the species. The consistency of the statistics implies that no other model parameter must be adjusted to compensate for the changing EOD signal; the modelled P-units produce the same defining qualitative behaviour at any EOD frequency.

The low magnitudes of spike correlation in the absence of external input are as expected intuitively since the multiple realisations at a particular frequency use unique sequences of random numbers, hence the sequences of EOD cycles on which spikes occur are different for each realisation. Thus the spike correlation should be very weak because the neurons have no common input apart from the EOD, and the noise randomly scrambles the EOD cycles on which firings occur independently for each neuron.

Gauging the effect of the bias on the model's behaviour was a natural next choice: it is the simplest parameter that will tune the strength of the input signal, adjusting it in a straightforward additive manner (Equation 3.2). The simulations yielded a nearly straight-line relationship between the input bias and mean firing rate of the receptors (Figure 3.3). The lag-1 ISI

correlations agree with the experimental range of values for the most part, with moderately negative values for a broad range of firing rates, except at the extreme firing rates where the correlations tend toward low magnitudes. However, the severe broadening of the EOD phase-lock as bias increases is atypical for dynamical systems such as neurons, since a stronger bias usually leads to a narrower range of phases on which firings occur, because it overcomes the noise, which is responsible for the phase jitter. An extra piece of information gained from the analysis is that the minimal ISI correlation occurs with no bias in the input.

Simulations with a high level of bias were also performed for various EOD frequencies (Figure 3.6), and confirmed the broadening of the EOD phase-lock distributions over this domain as well. However, they also foreshadowed the resonance-induced synchrony enhancement, or RISE effect (peaks in spike correlation curves) of the beat stimulus simulations (figures of Chapter 5), but on a much smaller scale (ratio of spike correlation values of about 1:100). The mechanism behind this RISE is the same as that underlying the numerically observed resonance of a neuron when its mean firing rate was in a simple ratio to the beat frequency. This was observed in Figure 3.6, as the neurons firing with a rate very near 450 Hz resonated with an EOD signal

with a frequency of 900 Hz producing a peak in the spike correlation.

The threshold time constant $\tau_\theta$ is another model parameter known from the theory to be a good candidate for tuning the firing rate in the simulations. Its inverse relation to the threshold rate of change produces slower approaches to meet the membrane potential level as $\tau_\theta$ increases. Therefore, the durations between action potentials get longer resulting in smaller firing rates (Figure 3.7). The simulations not only confirmed the theory, but also generated very good ISI correlations and produced very little variation in the EOD phase-lock for a similar range of firing rates as for exploring bias.

Since the threshold increment $\Delta\theta$ also determines the length of time between spikes by setting the threshold value immediately following a spike, it can also be used to choose the firing rate of the neurons. It, too, like the threshold time constant, has an inverse relation to the firing rate (Figure 3.8), as a larger increment prolongs the decay time of the threshold until it meets the membrane potential, thus delaying the next spike and decreasing the firing rate. In baseline simulations, a similar range of firing rates were produced as with varying the threshold time constant. A comparably low spread of EOD phase-lock was also recorded. The lag-1 ISI correlations in general are slightly lower in magnitude compared to those obtained when

the threshold time constant was varied. To generate P-unit behaviour with a significant negative lag-1 ISI correlation and a range of firing rates, then this study suggests that this would be better achieved using the threshold time constant rather than its increment.

At this point, there does not appear to be a single choice of parameter whose variation would enable the generation of the experimentally observed lognormal distribution of p-values [14]; this issue requires further investigation.

## 6.2 Linearity of Signal Coding

The envelope (Equation 2.5) extracted from a narrowband Gaussian noise signal via the Hilbert transform (Equation 2.6) is nonlinear since it is derived with a nonlinear process. A neuron whose firings have a high level of linear coherence (Equation 2.9) with such a nonlinear signal is said to exhibit one form of nonlinear coding. (This term is also used when the stimulus-response coherence to a signal is weak, but the response-response coherence is stronger [24].) It was shown in Figure 4.1D that the P-unit model presented in this study can function with a nonlinear coding scheme by showing significant

coherence to the envelope in the frequency range where the envelope has power in its spectrum. This effect was hypothesised to be related to the neuron's rheobase—the critical input strength below which the cell will not fire—and the nature of its firing rate-to-input strength relation, or $f$-$I$ curve, namely its degree of nonlinearity. This hypothesis was tested and shown to be valid because the model could be *linearised* (that is, made to perform linear coding). This was accomplished by smoothing out the $f$-$I$ curve near rheobase with greater noise in the system, or by avoiding the critical threshold altogether with a biased input signal, which moved the stimulation away into the more linear region of the $f$-$I$ curve above threshold. Both tests resulted in the absence of significant coherence to the signal envelope, but left the coherence to the signal itself intact, thus the neuron was only capable of linear coding.

The effect of the bias was also validated in recent experiments showing an inverse relationship between firing rate and nonlinearity of signal coding by the electroreceptors [25]. The agreement with the prediction made in this study is understandable from the model, since its firing rate increases with bias. This operation away from threshold in turn decreases the nonlinearity, as expected. It is thus clear that peripheral neurons can perform nonlinear

"envelope" coding when they are driven sufficiently strongly, which occurs, for example, when fish are very near one another.

## 6.3 Communication

The communication signals between the weakly electric fish studied in this work were 1) the passive beats, produced by the superposition property of waves and no other interaction between the fish other than being in the vicinity of each other, and 2) the active chirps, requiring an intentional alteration of the EOD frequency by one fish, which in turn causes a change in the resulting beating pattern. Their contributions to the synchrony of the electroreceptors are explored next.

### 6.3.1 Passive/Trivial Communication: Beats

The beat signal tends to synchronise electroreceptors with similar properties. The level of synchronisation, determined by measuring the spike correlation, strongly depends on several parameters of the P-unit model, as explored in Chapter 5.

Exploring the magnitude of the synaptic noise parameter $\sigma$ was a natural

first choice as this parameter separates the deterministic class of models from the (generally more realistic) stochastic class. The tendency of increasing noise to reduce the synchrony of neuronal responses is intuitive as higher noise produces higher variability in the evolution of a simulated response, thus reducing the probability of coincident spikes in membrane potential. The unexpected peaks in spike correlation near certain beat frequencies (for example, Figure 5.1) were shown to relate to resonances between the model's mean firing rate and harmonics of the beat—the RISE effect; this is believed to be a novel result. This correspondence can be explained by a higher tendency for the neurons to synchronise to the beat, thereby increasing the likelihood of their synchronising with each other.

The persistence of the synchrony peaks in spite of diminishing signal strength (contrast $c$) correlates with the assumption of the electroreceptors resonating with the beat. With a weakened effect of beats at low contrast, a true resonance effect occurs at harmonics and subharmonics of the neuron's intrinsic baseline firing rate. This synchronisation to the beat synchronises neurons with similar baseline properties.

The theory of resonance-induced synchrony enhancement is also corroborated by the fact that the peak locations in the spike correlation curve can

be shifted to other beat frequencies by changing the baseline firing rate of the neuron model with either the input bias parameter or the threshold time constant. As the firing rate changes, it corresponds to the harmonics of different beat frequencies. This is illustrated in Figure 5.1—and those that follow—by the shifting intersections of the firing rate curves and the lines of beat frequency multiples. The peaks coincide with these intersections quite consistently. It was also shown (Figure 5.3) that at high levels of bias the spike correlation is generally reduced by up to 30%, whereas the resonance peaks are eliminated completely. The overall reduction in correlation might be attributed to a smaller relative size of the beat compared to the increased average intensity of the biased input. The situation is analogous to an effective decrease in the signal contrast. However, by this analogy, the resonance peaks should be largely unaffected as observed by directly varying the contrast parameter $c$.

The extent of synchrony enhancement by resonance can also be suppressed with stochastic variability, or jitter, in the threshold increment, denoted by $\sigma_{\Delta\theta}$. It was shown that the peaks in spike correlation corresponding to the resonance frequencies can be reduced by increasing $\sigma_{\Delta\theta}$ without reducing the normal correlation level at other beat frequencies (Figure 5.5).

With variability in the threshold increment, the successive values of instantaneous firing rates after each action potential fluctuate, thus destroying the resonance to the presented beat signal. However, because the deviations are centered around zero, they get averaged out and produce no change to the *mean* firing rate, potentially preserving the general spike correlations at non-resonant beat frequencies as a result.

### 6.3.2 Active Communication: Chirps

Small chirps tend to synchronise similar electroreceptors while big chirps desynchronise them, at least momentarily in both cases [4]. In the former case, "synchronisation" is used in its weaker sense, since after a rapid upstroke in the beat caused by the chirp, there is a sharp increase in the firing rate (Figure 3.12). Consequently, there is a higher density of spikes at that moment that will increase the spike correlation slightly, but not nearly as significantly as the correlation *decreases* in the latter case (Figure 5.7). Also, in the rapid downstroke flavour of the small chirp, the neurons all cease to fire for a brief moment following the chirp, thus a spike correlation value is impossible to measure as there are no spikes with which to define its data set. Nevertheless, the exceptionally high (and low) firing rates during the

upstroke (and downstroke) are very valuable results that further solidify the importance of the P-unit's adaptation function. Possessing this property clearly indicates that the process of recognition of this type of active (that is, intentional) communication between the brown ghosts begins already at this early stage in the electrosensory neural pathway.

## 6.4 Future Study

As alluded to above, there are many forms the chirps can take, varying in characteristics such as the phase of the beat at which they occur as well as the amount by which the beat phase advances (from a small chirp), among others. The magnitude of the impact the chirps have on the P-unit response is also a function of the beat frequency [3]. Admittedly, the surface was merely scratched by this work in regards to this area of study.

A general outstanding question is how the P-units are able to produce such high spike correlations in experiment; the same levels were not reproduced in this study while having the model satisfy the stringent tests of reproducing a host of firing statistics. Perhaps another unknown mechanism is at work, and this is left for future study. The model nevertheless performs

qualitatively very well even if it does not achieve the same quantitative correlations.

Also, further study is necessary to determine the mechanism responsible for nullifying the resonance effect on the synchrony of P-units with high firing rates. This nullifying effect is recorded both in the simulations of the model presented here as well as in experimentation with the real P-units and may have implications on the fundamental properties of these sensory neurons.

Another direction is to understand the genesis of the lognormal distribution of p-values [14], and what this distribution implies for signal coding and processing in general, and for synchronisation in response to communication signals in particular. Future work can begin to address, using the methods developed herein, the spike correlation that results from combining the naturally-occurring diversity of receptors.

# Bibliography


[1] J Bastian. Electrolocation – I. How the electroreceptors of *Apteronotus albifrons* code for moving objects and other external stimuli. *J. Comp. Physiol. A*, 144:465–479, 1981.

[2] J Benda and AVM Herz. A universal model for spike-frequency adaptation. *Neural Comput.*, 15:2523–2564, 2003.

[3] J Benda, A Longtin, and L Maler. Spike-frequency adaptation separates transient communication signals from background oscillations. *J. Neurosci.*, 25(9):2312–2321, 2005.

[4] J Benda, A Longtin, and L Maler. A synchronization-desynchronization code for natural communication signals. *Neuron*, 52:347–358, 2006.

[5] J Benda, L Maler, and A Longtin. Linear versus nonlinear signal transmission in neuron models with adaptation currents or dynamic thresholds. *J. Neurophysiol.*, 104(5):2806–2820, 2010.

[6] CE Carr and MA Friedman. Evolution of time coding systems. *Neural Comput.*, 11(1):1–20, 1999.

[7] MJ Chacron. Nonlinear information processing in a model sensory system. *J. Neurophysiol.*, 95:2933–2946, 2006.

[8] MJ Chacron, A Longtin, and L Maler. Negative interspike interval correlations increase the neuronal capacity for encoding time-dependent stimuli. *J. Neurosci.*, 21(14):5328–5343, 2001.

[9] MJ Chacron, A Longtin, M St-Hilaire, and L Maler. Suprathreshold stochastic firing dynamics with memory in $p$-type electroreceptors. *Phys. Rev. Lett.*, 85(7):1576–1579, 2000.

[10] MJ Chacron, L Maler, and J Bastian. Electroreceptor neuron dynamics shape information transmission. *Nat. Neurosci.*, 8(5):673–678, 2005.

[11] DR Chialvo. How we hear what is not there: A neural mechanism for the missing fundamental illusion. *Chaos*, 13(4):1226–1230, 2003.

[12] B Ermentrout. Linearization of F-I curves by adaptation. *Neural Comput.*, 10:1721–1729, 1998.

[13] W Gerstner and WM Kistler. *Spiking Neuron Models: Single Neurons, Populations, Plasticity*. Cambridge University Press, 2002.

[14] D Gussin, J Benda, and L Maler. Limits of linear rate coding of dynamic stimuli by electroreceptor afferents. *J. Neurophysiol.*, 97(4):2917–2929, 2007.

[15] D Hansel, G Mato, C Meunier, and L Neltner. On numerical simulations of integrate-and-fire neural networks. *Neural Comput.*, 10:467–483, 1998.

[16] AL Hodgkin and AF Huxley. A quantitative description of membrane current and its application to conduction and excitation in nerve. *J. Physiol.*, 117:500–544, 1952.

[17] B Lindner and L Schimansky-Geier. Transmission of noise coded versus additive signals through a neuronal ensemble. *Phys. Rev. Lett.*, 86(14):2934–2937, 2001.

[18] A Longtin, JW Middleton, J Cieniak, and L Maler. Neural dynamics of envelope coding. *Math. Biosci.*, 214:87–99, 2008.

[19] A Longtin and M St-Hilaire. Encoding carrier amplitude modulations via stochastic phase synchronization. *Intern. J. Bifurc. Chaos*, 10(10):2447–2463, 2000.

[20] JW Middleton, E Harvey-Girard, L Maler, and A Longtin. Envelope gating and noise shaping in populations of noisy neurons. *Phys. Rev. E*, 75(2):021918, 2007.

[21] JW Middleton, A Longtin, J Benda, and L Maler. The cellular basis for parallel neural transmission of a high-frequency stimulus and its low-frequency envelope. *Proc. Natl. Acad. Sci. USA*, 103(39):14596–14601, 2006.

[22] JW Middleton, A Longtin, J Benda, and L Maler. Postsynaptic receptive field size and spike threshold determine encoding of high-frequency information via sensitivity to synchronous presynaptic activity. *J. Neurophysiol.*, 101(3):1160–1170, 2009.

[23] ME Nelson, Z Xu, and JR Payne. Characterization and modeling of P-type electrosensory afferent responses to amplitude modulations in a wave-type electric fish. *J. Comp. Physiol. A*, 181:532–544, 1997.

[24] JC Roddey, B Girish, and JP Miller. Assessing the performance of neural encoding models in the presence of noise. *J. Comput. Neurosci.*, 8(2):95–112, 2000.

[25] M Savard, R Krahe, and MJ Chacron. Neural heterogeneities influence envelope and temporal coding at the sensory periphery. *Neuroscience*, 172:270–284, 2011.

[26] M St-Hilaire and A Longtin. Coding of information in models of tuberous electroreceptors. *Math. Biosci.*, 188:157–174, 2004.

[27] R Wessel, C Koch, and F Gabbiani. Coding of time-varying electric field amplitude modulations in a wave-type electric fish. *J. Neurophysiol.*, 75(6):2280–2293, 1996.

[28] HH Zakon. The electroreceptive periphery. In TH Bullock and W Heilingenberg, editors, *Electroreception*, page 103. John Wiley and Sons, 1986.